# Accelerated learning and co-optimization of elastocaloric effect and stress hysteresis of elastocaloric alloys

Shiyu He<sup>1,2</sup>, Fei Xiao<sup>1,3,6\*</sup>, Ruihang Hou<sup>1</sup>, Shungui Zuo<sup>1</sup>, Ying Zhou<sup>1</sup>, Xiaorong Cai<sup>1</sup>, Zhu Li<sup>1</sup>, Yanming Wang<sup>4</sup>, Aysu Catal Isik<sup>5</sup>, Enrique Galindo-Nava<sup>5</sup>, Xuejun Jin<sup>1,3\*\*</sup>

<sup>1</sup>State Key Lab of Metal Matrix Composite, School of Materials Science and Engineering, Shanghai Jiao Tong University, 800 Dong Chuan Road, Shanghai 200240, P. R. China

<sup>2</sup>Materials Genome Initiative Center, Shanghai Jiao Tong University, Shanghai 200240, China

<sup>3</sup>Institute of Medical Robotics, Shanghai Jiao Tong University, Shanghai 200240, China <sup>4</sup>University of Michigan-Shanghai Jiao Tong University Joint Institute, Shanghai Jiao Tong University, 800 Dong Chuan Road, Minhang District, Shanghai 200240, China <sup>5</sup>Department of Mechanical Engineering, University College London, Torrington Place, London WC1E 7JE, United Kingdom

<sup>6</sup>Department of Materials Science and Engineering, Graduate School of Engineering, Osaka University, 2-1, Yamada-oka, Suita, Osaka 565-0871, Japan

1

<sup>\*</sup> Corresponding author. Tel.: +86 21 54745567. E-mail address: xfei@sjtu.edu.cn (F. Xiao).

<sup>\*\*</sup> Corresponding author. Tel.: +86 21 54745560

E-mail address: jin@sjtu.edu.cn (X. Jin).

#### **Abstract**

Elastocaloric alloys stand as the preferred technology for non-vapor-compression refrigeration. Here, we present a machine learning (ML) framework to accelerate the development of novel elastocaloric alloys with large adiabatic temperature change ( $\triangle$  $T_{\rm ad}$ ) and low stress hysteresis ( $\triangle \sigma_{\rm hy}$ ). The comprehensive framework comprises database construction, feature selection, model construction, alloy design and validation, and model interpretation. Features are selected according to the physical attributes they represent. Properties that may reflect the compatibility between parent and product phases, lattice distortion, and the free energy in the alloy are considered in the model. Among them, the key features are screening by recursive feature elimination and exhaustive search methods. The trained models in combination with the Bayesian optimization method are exploited to achieve multi-objective optimization. Using the results, a newly designed elastocaloric alloy shows a large adiabatic temperature change of 15.2 K and low average stress hysteresis of 70.3 MPa at room temperature, which is consistent with our predictions. The predictions of our ML model are interpreted by the Shapley Additive exPlainations (SHAP) approach, which explicitly quantifies the effects of each feature in our model on the adiabatic temperature change and stress hysteresis. Additionally, we employ the Sure-Independence Screening and Sparsifying Operator (SISSO) method in conjunction with the key features to formulate explicit  $\triangle$  $T_{\rm ad}$ -SISSO and  $\triangle \sigma_{\rm hy}$ -SISSO model. The optimal SISSO model agree with the finding derived from the SHAP analysis. Our work represents a starting platform for the digital design of innovative alloys with optimized properties for elastocaloric applications.

**Keywords:** Elastocaloric alloys, Adiabatic temperature change, Stress hysteresis, Machine learning, Multi-objective optimization

#### 1. Introduction

Vapor-compression refrigeration based on hydrocarbon has gained widespread utilization in improving human daily lives such as home air conditioning systems [1]. However, vapor-compression technology with high energy consumption contributes to global warming and ozone depletion and poses a major challenge to environmental sustainability [2-4]. As the world strives for carbon neutrality and environmental protection, scientists have developed a growing interest in environment-friendly and energy-efficient novel cooling technologies based on, magnetocaloric [5], elastocaloric [6] and electrocaloric refrigeration [7, 8]. According to a comprehensive report by the United States Department of Energy, the elastocaloric system based on TiNi shape memory alloys (SMAs) has emerged as a highly recommended approach for non-vapor-compression refrigeration [9-12]. Most recently, Qian et al. [13] demonstrated a high-efficiency elastocaloric cooling system incorporating nitinol tubes, showing remarkable and exceptional cooling performance.

The phenomenon of elastocaloric effect (eCE) is closely associated with stress-induced thermoelastic martensitic transformation, wherein the adiabatic temperature change or the isothermal entropy change serves as prominent characterization parameters [11, 14-16]. Under the influence of mechanical loading, the parent phase (austenite) undergoes a transition to the martensitic phase, thereby increasing the environmental temperature with the release of latent heat. Conversely, during unloading, the reverse martensitic transformation occurs, resulting in the absorption of heat from the surrounding environment, thus enabling solid-state cooling. Until now, there are several SMAs including TiNi-based [17-19], Cu-based [20-25], Co-based [15, 26], and Heusler alloys [16, 27-33]. TiNi-based alloys have been successfully used as critical materials for caloric cooling prototypes due to their promising elastocaloric capacity [13, 29, 34-36]. However, TiNi alloys possess a high stress hysteresis, which gives rise to the accumulation of defects and suppresses the reversibility of martensitic transformation [29, 37, 38]. Stress hysteresis is related to the macroscopic manifestation of energy dissipation during phase transformation. In general, SMAs with a small

hysteresis can acquire high energy conversion efficiency and low fatigue due to small energy loss and favorable transformation compatibility. It is well known that the addition of third elements such as Fe, Pd, Co, and Cu will adjust the hysteresis [29, 37, 39, 40]. Nevertheless, several published studies have indicated that the elastocaloric effect has a tendency to decrease when third elements are added [10, 34, 37, 41, 42]. Therefore, achieving a balance between the elastocaloric effects and hysteresis is of utmost importance in the design of novel TiNi-based shape memory alloys.

The primary objective of computational material design approaches is to employ both conceptual and numerical approaches to predict the composition, structure, and properties of materials and use the models to design new ones with improved performance [43]. Conventional material design approaches relying on trial and error [44, 45] prove to be inefficient and costly, especially when confronted with the challenge of multi-objective optimization from a large pool of data from candidate materials [46, 47]. With the advancement of artificial intelligence, data-driven machine learning methods provide a tremendous boost to accelerate material discovery [48-52]. Extensive research efforts have substantiated the potential of machine learning in designing shape memory alloys with desired properties. Peltier et al. [53], Udesh et al. [54], and Xue et al. [55] used machine learning to study the relationships between alloy composition and martensitic phase transformation and develop novel high-temperature shape memory alloys (HTSMAs). Lookman et al. [56] designed shape memory alloys with ultra-low thermal hysteresis by active learning. Pang et al. [57] developed shape memory ceramics with low thermal hysteresis by polynomial machine learning algorithm in combination with CALPHAD. Tian et al. [58] and Ding et al. [59] exploited machine learning to predict the elastocaloric effect. These studies have predominantly concentrated on optimizing a single property, whereas material design often necessitates the consideration of multiple properties. Machine learning coupled with multi-objective optimization methodologies has been established as an effective approach for addressing multiple properties. For instance, Gopakumar et al. [60] employed an adaptive design strategy to optimize the thermal hysteresis and transition

temperature of shape memory alloys (SMAs). Solomou et al. [61] devised a framework for efficiently discovering precipitation-strengthened NiTi shape memory alloys possessing three desired properties using Bayesian methods. Despite data-driven models significantly advancing the discovery of SMAs with desirable thermodynamic properties, scant attention has been devoted to stress hysteresis behavior.

In this work, we develop a co-optimization framework for accelerating the design of new TiNi-based shape memory alloys with a satisfactory combination of adiabatic temperature change and stress hysteresis using Bayesian multi-objective optimization and machine learning techniques. We synthesize a novel alloy and measure its transformation properties to validate our computational framework. In addition, we utilize the Shapley Additive Explanation (SHAP) and Sure Independent Screening and Sparsifying Operator (SISSO) technique to analytically interpret the relationships between selected features and electrocaloric properties in the black-box models. The last section presents further discussion and the conclusions arising from this work.

## 2. Methodology

The design strategy of novel SMAs with the desired combination of adiabatic temperature change and hysteresis based on the machine learning method is shown in **Fig. 1**. There are five modules including database construction, feature selection, model construction, alloy design and validation, and model interpretation.

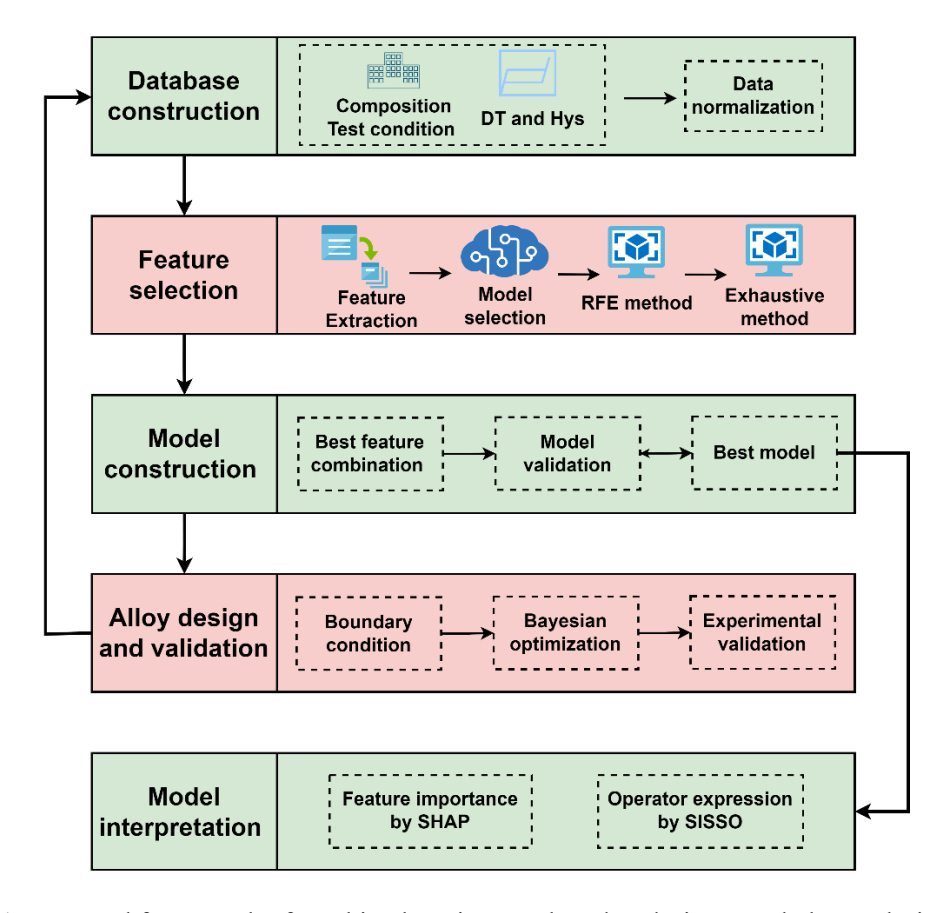


**Fig. 1.** Proposed framework of machine learning employed to design novel elastocaloric alloys with desired adiabatic temperature change and stress hysteresis.

### 2.1 Database construction

The performance of machine learning significantly depends on the quality of the database used. A reliable database enables the acquisition of data models with both high accuracy and generalization capabilities. The experimental information of adiabatic temperature change and stress hysteresis for SMAs is highly dispersed and limited, especially for TiNi-based alloys. To minimize the uncertainties introduced by experiments as much as possible, we adopt a selection criterion that focuses on bulk SMAs with similar fabrication processes including vacuum melting, homogenization treatment, and aging treatment. The test temperature and loading condition are also used as input variables to construct the prediction model because they are strongly associated with adiabatic temperature changes. We collect 137 alloy data with adiabatic temperature change ( $\triangle T_{\rm ad}$ ) and 60 alloy data with average stress hysteresis ( $\triangle \sigma_{\rm hy}$ ) [5,

9-11, 13, 14, 17, 20, 26, 34, 37, 41, 42, 59, 62-77]. It is worth noting that  $\triangle T_{ad}$  represents the absolute value of the adiabatic temperature change during cooling. Then the data preprocessing is used to eliminate the influence of different data dimensions on the convergence speed and accuracy of the model. Specifically, predictive models that utilize distance metrics, such as support vector machines (SVM) and decision trees, are highly sensitive to disparities in feature dimensionality. In this work, we adopt a data normalization process to eliminate the dimensionality of variables. The formula is as follows:

$$X_{norm} = \frac{X - X_{min}}{X_{max} - X_{min}} \tag{1}$$

Where X is the feature value,  $X_{min}$  is the minimum feature value,  $X_{max}$  is the maximum feature value,  $X_{norm}$  is the standardized feature value.

#### 2.2 Feature selection

Alloy design based on machine learning requires selecting relevant alloy features and connecting them to their chemical composition. Alloy properties are considered akin to fingerprints, establishing a strong connection with the properties of the alloy. Developing reliable prediction models based on alloy features to improve design predictability has been highlighted by numerous scholars [47, 54, 78, 79]. In addition to the three test parameters (test temperature, stress, strain rate), we use the matminer toolkit [80] to extract 23 alloy features comprising atomic features and physical parameters from alloy composition. Atomic features such as atomic radii and atomic number are inherent physical and chemical attributes of individual alloy constituents, while alloy parameters such as phase fraction originate from specific parameter formulas. Details of all features are listed in the **Supplementary material**. Considering the potential risk of overfitting associated with an excessive number of features, we employ feature selection methods comprising correlation analysis, recursive feature elimination, and exhaustive search methods to systematically search for the optimal combination of features.

#### 2.3 Model construction

Three classical machine learning methods, extreme gradient boosting (XGBT), support vector regression (SVR), and random forest (RF) are utilized to evaluate the predictive capability of the model. We randomly divided 80% of the database as the training set and allocated 20% as the test set. The complexity and diversity of the model parameters provide a broad spectrum of possibilities for optimizing the model performance. Indeed, finding the optimal balance between model parameters is a challenging task. In this work, we use a fast search method [81] in combination with Leave-One-Out (LOO) to determine the best parameter group. The fundamental concept behind the LOO method involves dividing the dataset into k subsets, with each subset containing a single test sample, where k corresponds to the size of the dataset. These data partitioning methods contribute to assessing the generalization ability of machine learning models trained on small samples. Furthermore, the Root Mean Square Error (RMSE) and Pearson correlation coefficient R are used to evaluate the accuracy of the model.

# 2.4 Alloy design and validation

Machine learning models can facilitate the direct search for shape memory alloys with desired adiabatic temperature changes or hysteresis within a defined compositional space. However, when the optimization involves simultaneously considering the combination of adiabatic temperature change and hysteresis, the task of developing a satisfactory alloy composition becomes more complex and challenging. We combine two predictive models with Bayesian optimization (BO) to achieve multi-objective optimization of the properties mentioned above [79, 82]. Bayesian optimization (BO) is a strategy used for black-box optimization, where the scalar function to be optimized (sometimes referred to as the oracle) may be non-differentiable or difficult to evaluate (computationally expensive). The optimization principle of adiabatic temperature change and hysteresis with BO method is presented in **Fig. 2**, which mainly comprises alloy composition boundary conditions, composition candidate search and score,

property prediction, and stop criteria. To validate the calculations, an optimal alloy candidate was synthesized and prepared using vacuum induction melting in a graphite crucible. A detailed fabrication process has been described in our previous work [42].

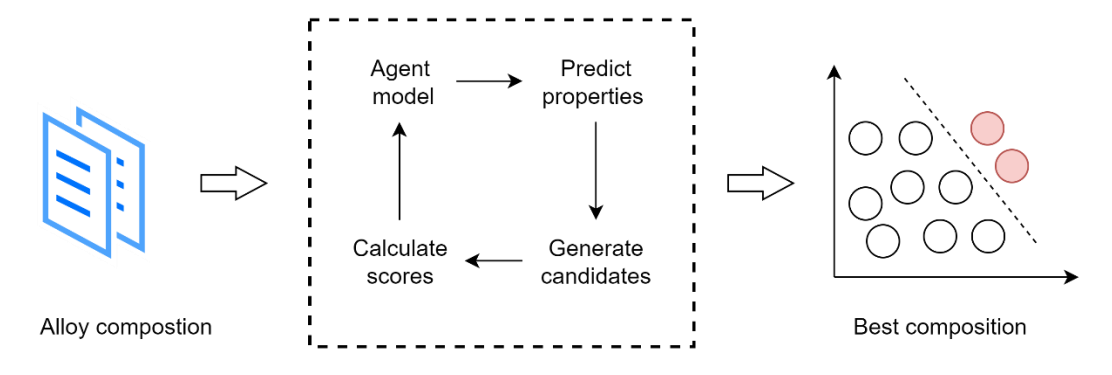


Fig. 2. Schematic of the computational workflow of Bayesian optimization.

# 2.5 Model interpretation

While the black-box model approach in Machine Learning has been extensively employed in material design, demonstrating accuracy in predicting material properties, it is often challenging to identify explicit correlations between input features and alloy properties. SHAP (SHapley Additive exPlanations) [83] is a game theory approach that elucidates the importance of each feature on the output of any machine learning model. This method involves calculating the marginal contribution of features to the overall output of the model and subsequently provides an indirect understanding of the "black box model" from both a global and local perspective. The importance of key features is calculated and the effects of key alloy features on adiabatic temperature change and hysteresis is determined by SHAP in this work. Another approach to understanding the relationship between inputs and output is using an interpretable white-box model such as SISSO [84] (Sure Independent Screening and Sparsifying Operator). SISSO is a datadriven approach that combines symbolic regression and compressed sensing to identify models and descriptors in explicit mathematical expressions for materials science. Although symbolic regression can establish more easily interpretable analytical equations, discovering the optimal combination of mathematical operators from a large number of features is still a significant challenge. To mitigate the computational cost associated with symbolic regression, we utilize the aforementioned feature selection method to obtain an optimal combination of features. Subsequently, we derive the explicit formulas for adiabatic temperature change and hysteresis by integrating the best feature group with the SISSO method.

#### 3. Results

## 3.1 Feature selection and modeling

Pearson product-moment correlation coefficient (R) quantifies the level of correlation between two variables. A high absolute value of R, close to 1, indicates a strong linear correlation between the variables. Thus, the correlation coefficient can be used to evaluate the linear relationship calculation between alloy features and target properties and to eliminate redundant features that exhibit highly linear correlations. The correlation coefficients of adiabatic temperature change and hysteresis are presented in **Fig. 3**, where a lighter color indicates a stronger linear relationship. Many alloy features exhibit weak linear correlations with adiabatic temperature change and hysteresis. The maximum absolute correlation coefficients (|R| values) are less than 0.6, suggesting the presence of a non-linear relationship between alloy features and these two properties. Furthermore, the maximum |R| values between alloy features are less than 0.95, which falls short of the threshold for feature elimination.

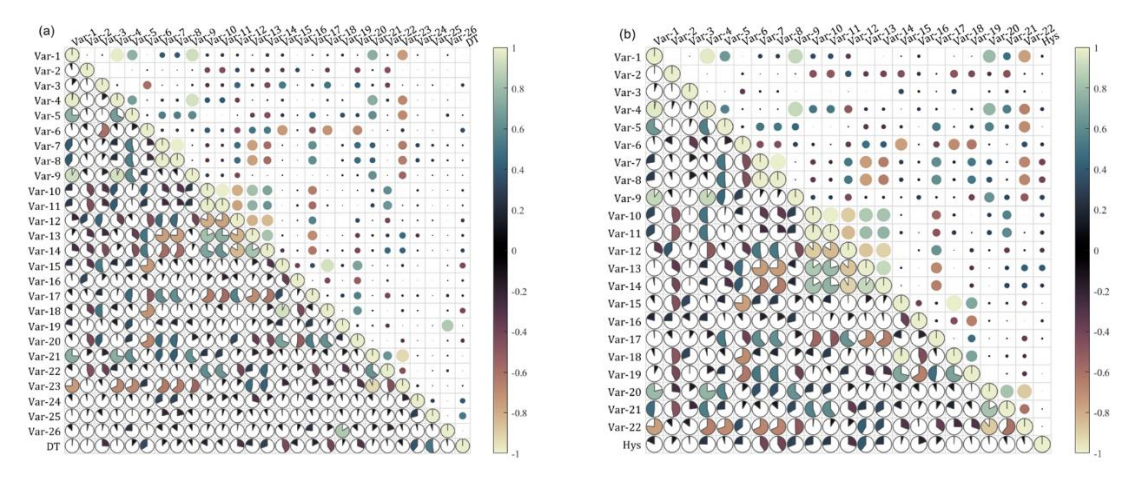
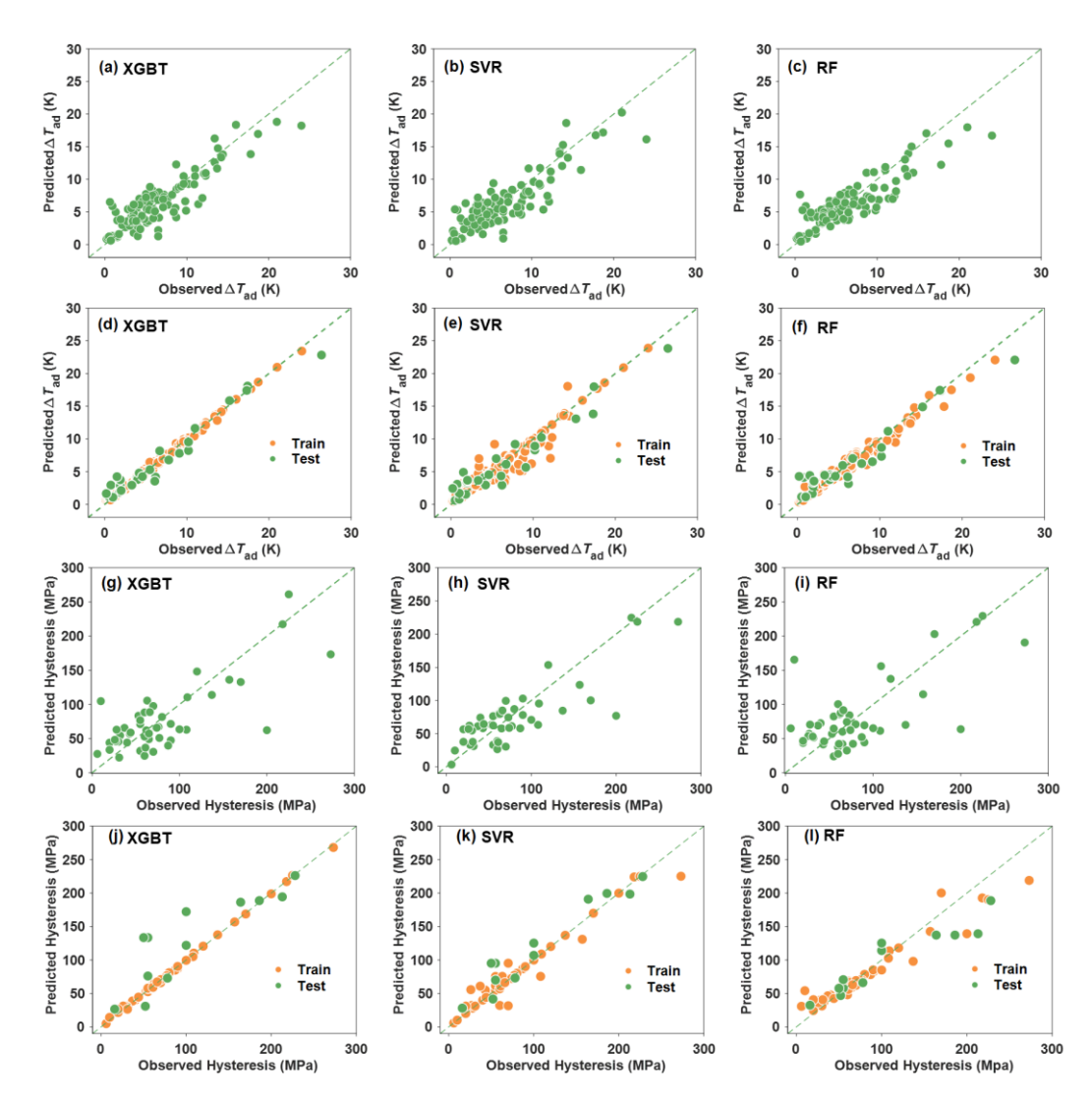


Fig. 3. Feature processing based on the correlation coefficients. (a) Adiabatic temperature change.

(b) Average stress hysteresis.

To reduce the complexity of the machine learning model, the recursive feature elimination with cross-validation (RFECV) method is employed to eliminate dimensions of alloy features. RFECV is to select features by recursively considering smaller and smaller sets of features and computing the cross-validated scores. This approach involves two steps: model selection and feature elimination. The selection of an appropriate model is of utmost importance when considering subsequent feature selection. As shown in Fig. 4, three models based on XGBT, SVR, and RF methods are used to predict the adiabatic temperature change and hysteresis. We use the training set with cross-validation to determine the best combination of model parameters, and then test the model performance. Fig. 4 (a)-(f) depict the comparisons between measured and predicted adiabatic temperature change. The cross-validations of the three models show similar results where several predictions deviate significantly from the experimental results. The training and testing results indicate the XGBT model performs better compared with the other models. Fig. 4 (g)-(l) presents the machine learning results of average stress hysteresis. There are subpar performances for the three models where most predictions are inconsistent with the measurements. However, the SVR model presents an adequate performance where the predictions mostly agree with experiments. We also calculate the RMSE and R values to demonstrate the performance of the three models. According to Fig. 5, It is evident that the XGBT-based adiabatic temperature change has the lowest RMSE of 1.39 K and the highest R of 0.98, while the SVR-based hysteresis has the lowest RMSE of 22.28 MPa and the highest R of 0.96. Thus, the XGBT and SVR models are used to eliminate the alloy features for adiabatic temperature change and hysteresis, respectively.



**Fig. 4.** Comparison between predicted values from different machine learning models and the observed values. (a)-(c) Cross-validation on train set of adiabatic temperature change. (d)-(f) Train and test set of adiabatic temperature change. (g)-(i) Cross-validation on train set of average stress hysteresis. (j)-(l) Train and test set of average stress hysteresis.

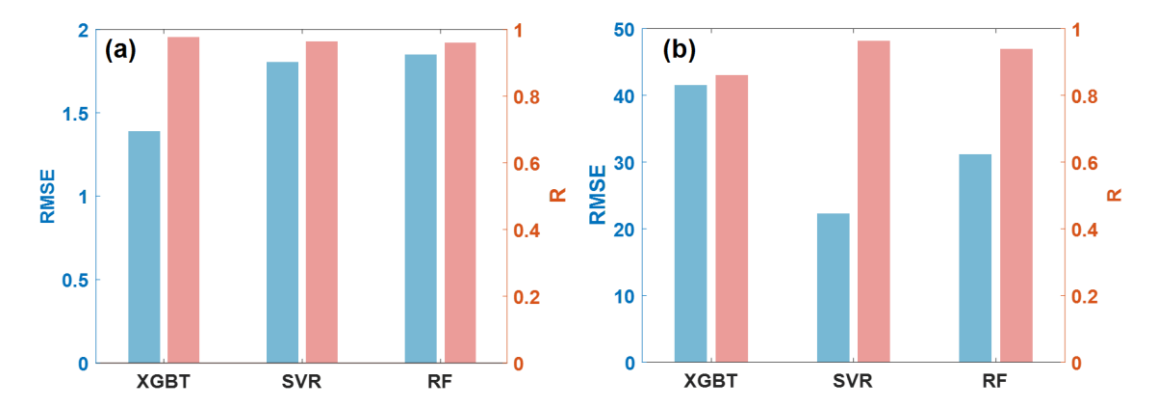
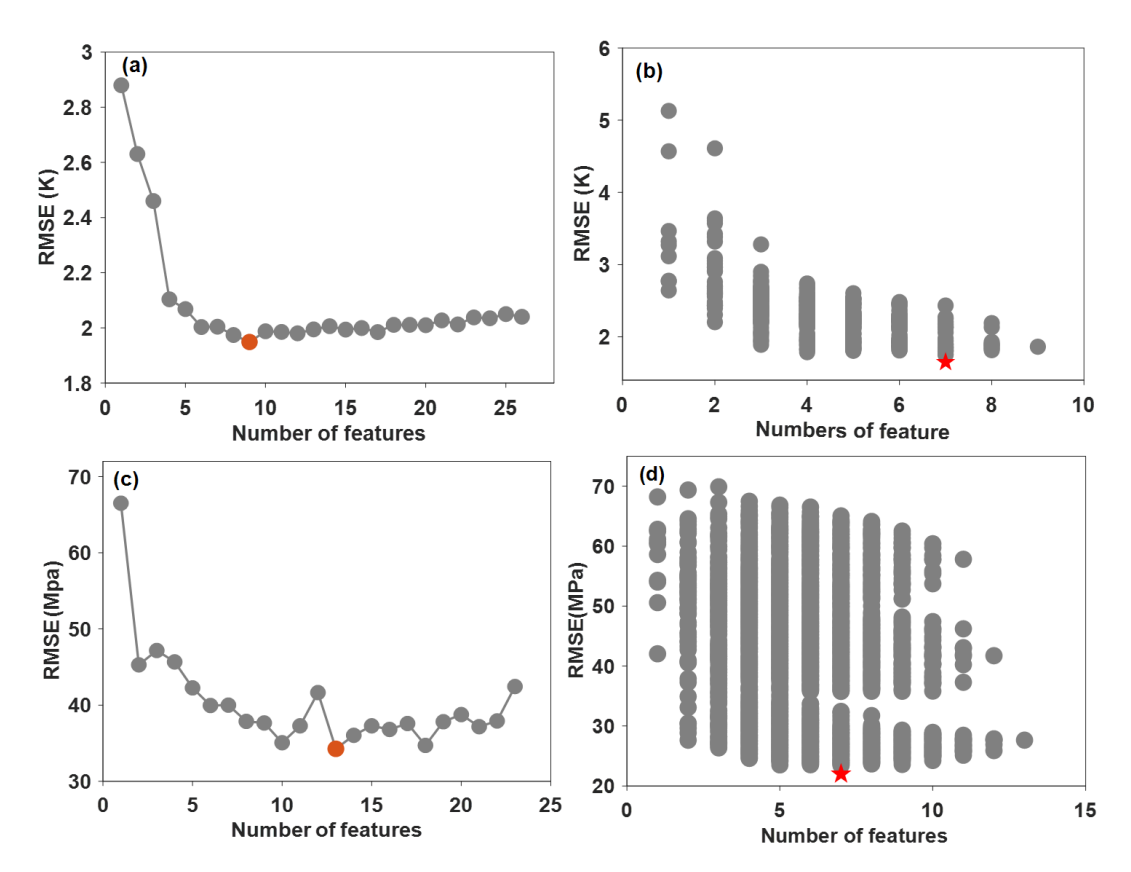


Fig. 5. Performance of different models on our test set. (a) Adiabatic temperature change. (b)

#### Average stress hysteresis.

Fig. 6 (a) and (b) depict the recursive feature elimination (RFE) process for adiabatic temperature change and stress hysteresis, respectively. The objective of recursive feature elimination is to adjust the number of features by systematically eliminating them based on their importance. In the figures, it is evident that as the number of features increases, the model's error initially decreases and then exhibits a tendency to increase. The optimal number of features for adiabatic temperature change is identified as 9, whereas for hysteresis, it is determined to be 13. The details of reserved features are listed in the supplementary information. To further reduce the number of features, an exhaustive search elimination (ESE)method is employed to identify the best combinations of features by using all the combinations of the remaining alloy factors from the RFE process. The results of feature selection using the exhaustive search elimination method for adiabatic temperature change are presented in Fig. 6 (c). The model's error initially decreases and then rises with the feature number increasing. The minimum error is achieved when the number of features is 7. The corresponding feature combination is as follows: APE (Atomic Packing Efficiency), CE (Configuration Entropy), VEC (Mean Valence Electron Concentration), SMM (Shear Modulus Mean), T (Test Temperature), ST (Stress), SR (Strain rate). As shown in Fig. 6 (d), When the number of features is 7, the model achieves the minimum error. The corresponding feature combination is as follows: YD (Yang Delta), RLM (Radii Local Mismatch), CE (Configuration Entropy), AWM (Mean Atomic Weight), ED (Electronegativity Delta), SMD (Shear Modulus Delta), SMSM (Shear Modulus Strength Model).



**Fig. 6**. Feature elimination to find the key features from the feature pool with recursive feature elimination and exhaustive search elimination. (a)-(b) Adiabatic temperature change. (c)-(d)

Average stress hysteresis.

After the feature selection procedure, we employ the XGBT algorithm for constructing the prediction model of adiabatic temperature change, and the Support Vector Regression (SVR) algorithm for constructing the prediction model of hysteresis. The performance of the machine learning model of adiabatic temperature change utilizing the XGBT algorithm is illustrated in **Fig. 7 (a) and (b)**. Notably, the training and testing data exhibit a close alignment along the diagonal (dashed line). The root mean squared error (RMSE) values for the training and testing data are reported as 0.32 K and 1.38 K, respectively, while the calculated R values are determined to be 0.99 and 0.97, respectively. These outcomes are indicative of a strong concordance between the model predictions and experimental observations. **Fig. 7 (c) and (d)** illustrate the distribution of data points evenly on both sides of the diagonal line for hysteresis. The RMSE values for the training and testing data are reported as 16.71 MPa and 9.23 MPa, respectively. Additionally, the R values are determined to be 0.99 and 0.96, respectively,

indicating good agreement between the predictions and experimental results within a reasonable error range. Considering the concern of overfitting, we employ cross-validation as a method to evaluate the model's generalization ability. Indeed, the cross-validation method with leave-one-out (LOOCV) is a recommended procedure for preventing overfitting. The cross-validation results for adiabatic temperature change and hysteresis are illustrated in **Fig. 7 (b)** and **(d)**. While there are a few data points that deviate from the diagonal line, the majority of predictions exhibit strong agreement with the experimental results. The RMSE of adiabatic temperature change and hysteresis are 1.75 K and 23.40 MPa, respectively, and the R values of adiabatic temperature change and hysteresis are 0.9352 and 0.9234, respectively. These scores indicate a favorable generalization ability of the model introduced in this study.

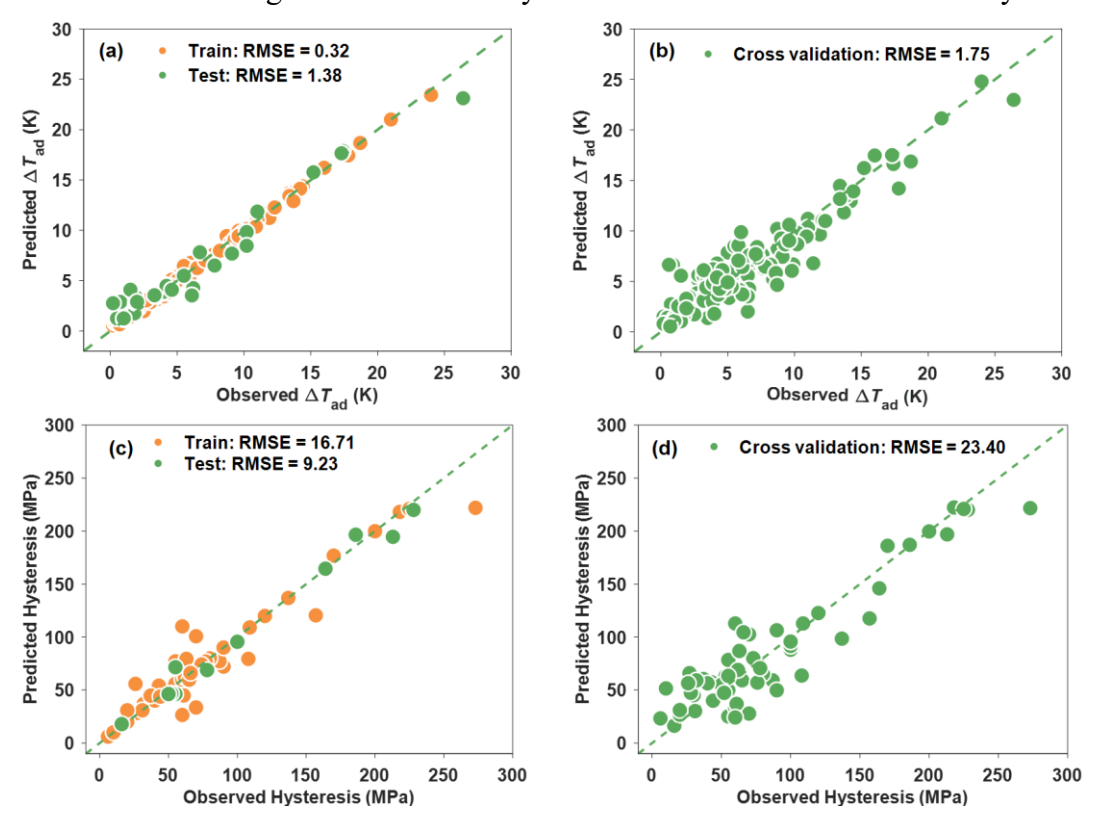


**Fig. 7.** The performance of the machine learning model with SVR algorithm on training, testing set, and LOOCV of all data. (a)-(b) Adiabatic temperature change. (c)-(d) Average stress hysteresis.

# 3.2 Alloy design and validation

The objective of our alloy design approach using a machine learning model is to

discover optimized alloy compositions that can achieve a balance between adiabatic temperature change and average stress hysteresis. It is well known that the hysteresis of SMAs can be adjusted by the addition of elements such as Fe, Pd, Co, and Cu [29, 37, 39, 40]. The incorporation of Cu into TiNi shape memory alloys (SMAs) has been extensively demonstrated to result in a reduced lattice mismatch and enhanced middle eigenvalue ( $\lambda_2$ ). The middle eigenvalue of the transformation stretch tensor between the parent and product phases,  $\lambda_2$ , is a crucial parameter to assess the crystallographical compatibility of these phases. Small lattice mismatch and a  $\lambda_2$  value closer to 1 usually indicate low stress hysteresis [85]. Thus, Cu is the first alloying element in our design criteria, other elements comprising Co, Fe, and Pd will be randomly selected by BO optimization. It is worth noting that small additions of third elements such as V, Zr, and Al are used to improve the mechanical properties of alloys [42, 86, 87]. The boundary condition is then set as  $\text{Ti}_a \text{Ni}_{100-a-b-c-d} A_b B_c C_d$ , where A is Cu, B can be Fe, Pd, Co, and C can be V, Zr, Hf, Al. As for their compositional range, a lies between 49.2 and 50, b lies between 1 and 10, c lies between 1 and 3, and d is within 0.1-1.

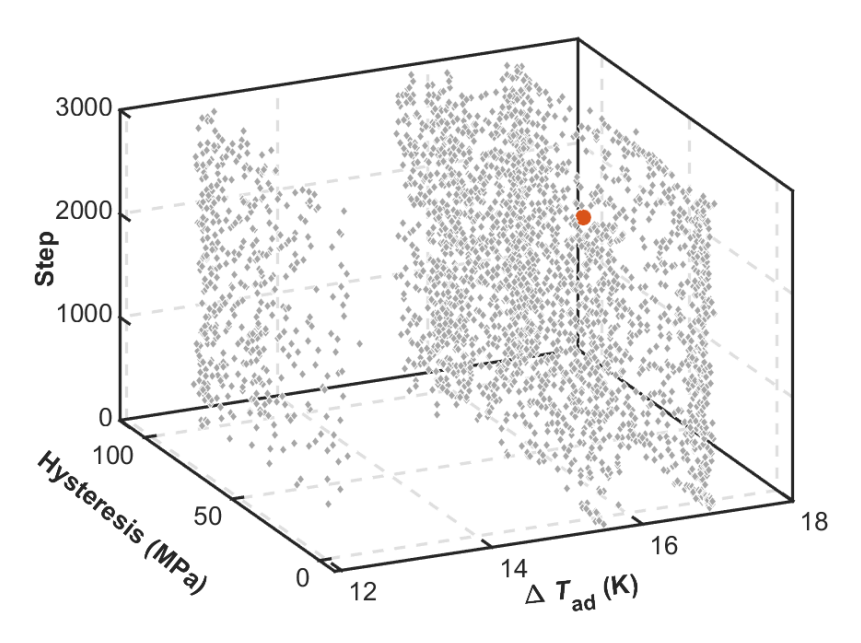


**Fig. 8**. The evolution of Bayesian optimization for adiabatic temperature change and average stress hysteresis. Red point represents the best composition.

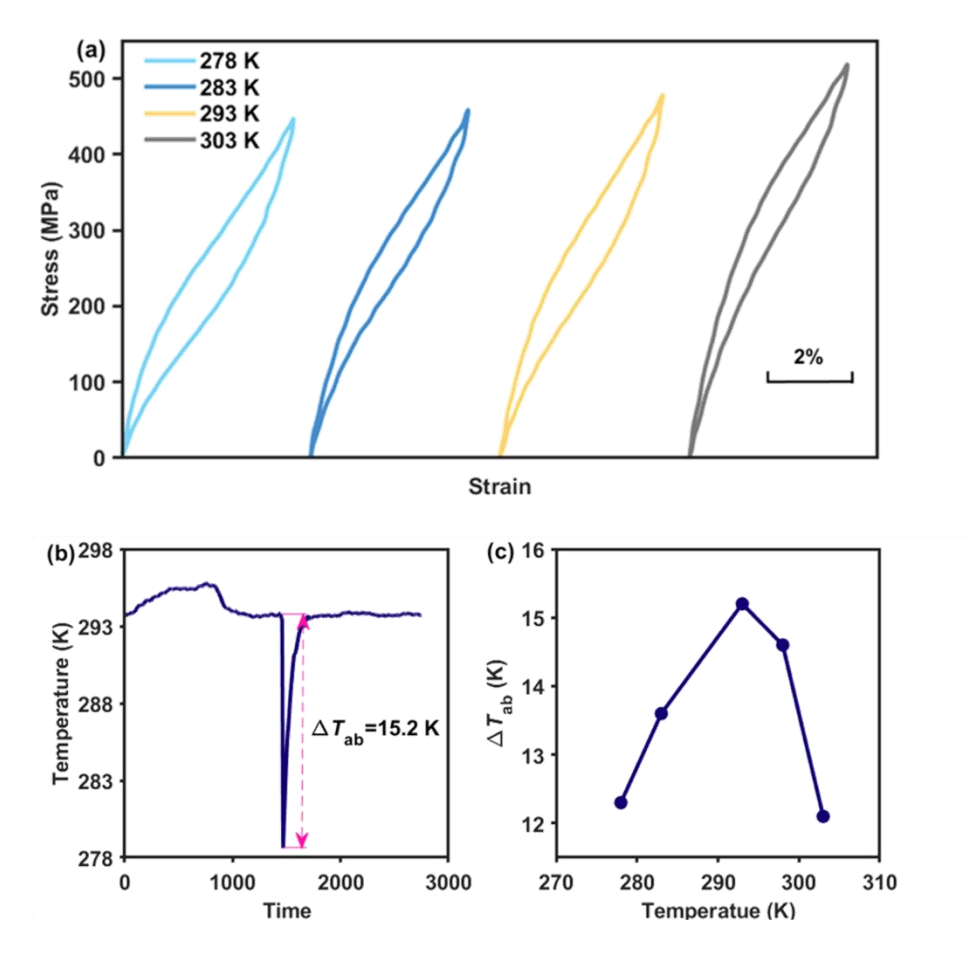


**Fig. 9.** Measurements of the newly designed alloy. (a) Tensile test results at different temperatures. (b) Transformation temperature changes with time at 293 K. (c) adiabatic temperature change at different testing temperatures.

**Fig. 8** illustrates the iterative process of Bayesian optimization, where the development of the optimal composition is conducted through continuous observation and updating of the estimate for the objective function. Based on the optimization result, Ti<sub>49,3</sub>Ni<sub>45,9</sub>Cu<sub>3,7</sub>Co<sub>1,0</sub>Zr<sub>0,1</sub> is identified as the optimal alloy composition. Subsequently, this composition is synthesized and prepared to validate the predictions made by our models. The fully recovered superelastic curves at temperatures from 278 K to 303 K are shown in **Fig. 9** (a). It is evident that the applied stress gradually increases as the testing temperature increases. The stress-strain curves exhibit small hysteresis loops, with stress hysteresis values of 76 MPa at 278 K, 65 MPa at 283 K, 74 MPa at 293 K, and 66 MPa at 303 K. Thus, the average stress hysteresis is 70.3 MPa. **Fig. 9** (c) shows the adiabatic temperate change at temperatures from 278 K to 303 K. The adiabatic temperature change exhibits an initial increase followed by a subsequent decrease as

the temperature rises. It reaches its peak value of 15.2 K at 293 K, as illustrated in the Fig. 9 (b).

Table. 1. Comparison of ML predictions and the experimentally measured adiabatic temperature change (in K) and average stress hysteresis (in MPa) for the designed synthesized samples.

Alloys	Property	Experiment	Calculation	Error
Ti49.3Ni45.9Cu3.7Co1.0Zr0.1	$\triangle T_{\mathrm{ad}}$	15.2	16.8	1.6
	$ riangle \sigma_{ m hy}$	70.3	83.1	12.8

A comparison of the predicted and measured adiabatic temperature change and hysteresis for the designed alloy is listed in **Table. 1**. The predicted adiabatic temperature change and hysteresis are 16.8 K and 83.1 MPa, respectively, which is consistent with the measured results. The absolute errors, amounting to 1.6 K and 12.8 MPa, fall within the acceptable range for model error. We also compare our designed alloy data with other results reported in the literature. As shown in **Fig. 10**, our new alloy exhibits large adiabatic temperature change and small hysteresis, achieving a good balance of the two competing properties. This result corroborates the effectiveness of our computational approach in designing novel elastocaloric shape memory alloys. In future research, we can adopt an iterative approach to improve our model and optimize the alloy composition cyclically for pushing the boundaries of performance and achieving superior performance characterized by exceedingly high adiabatic temperature change and extremely low hysteresis.

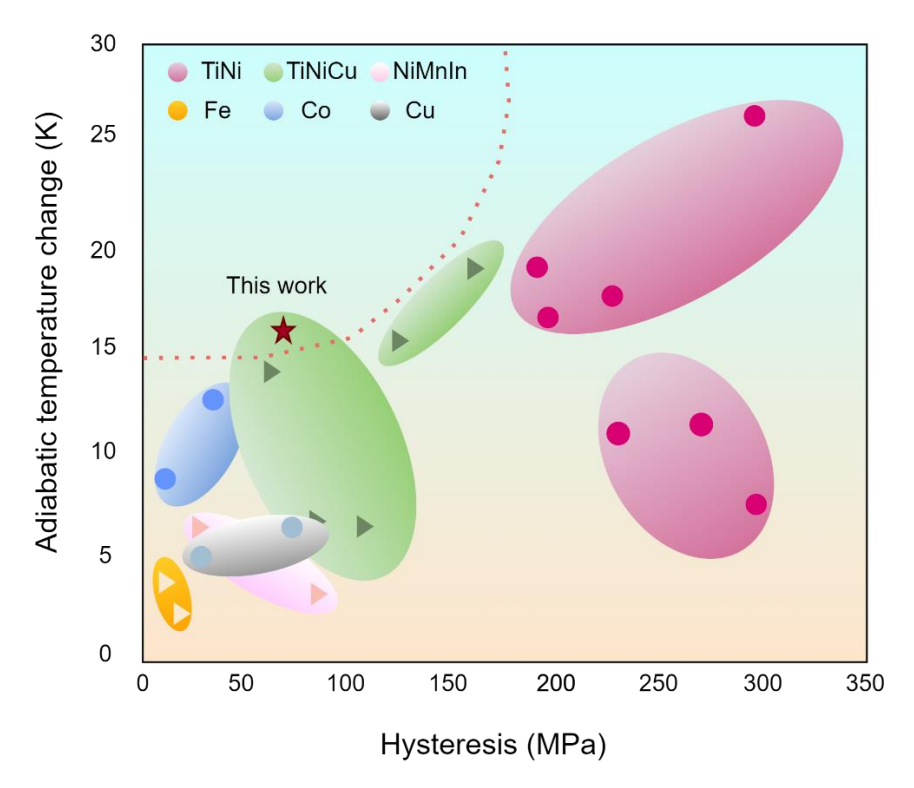


**Fig. 10**. Comparison of the adiabatic temperature change and stress hysteresis of our designed alloy with other reported bulk elastocaloric alloys [9, 22, 26, 29, 64, 68, 70, 88-91]. The red dashed line represents an optimal combination in alloy performance.

## 4. Discussion

# 4.1 Relationship between inputs and outputs using the SHAP method

The majority of machine learning models are based on a "black-box" approach that builds complex implicit relationships between inputs and outputs. This in turn hinders any physical insights into the phenomena under examination [84, 92]. it is imperative to employ alternative methods that aid in interpreting the black-box model to gain a deeper understanding of potential physical mechanisms involved in the transformation processes and to enhance the design of SMAs. In this work, SVR and XGBT models are regarded as black-box models owing to their ability to capture complex and implicit relationships between inputs and outputs. The inherent complexities of these models involve highly intricate relationships that are difficult to comprehend directly. Recently, Lundberg et al. [93] proposed a black-box

interpretability method known as SHAP (SHapley Additive exPlanations), which offers the capability to explain the outputs of any machine learning model, regardless of its complexity or black-box nature. SHAP provides valuable insights into the contributions of individual features in the model's output. It has been widely used to interpret the effect of relevant material features or alloy compositions on targeted properties. For example, He et al. [78] grasped the key features that influence the transformation temperature of high-entropy shape memory alloys and investigated the impact rule of electronegativity and atomic radius differences on the phase transition temperature.

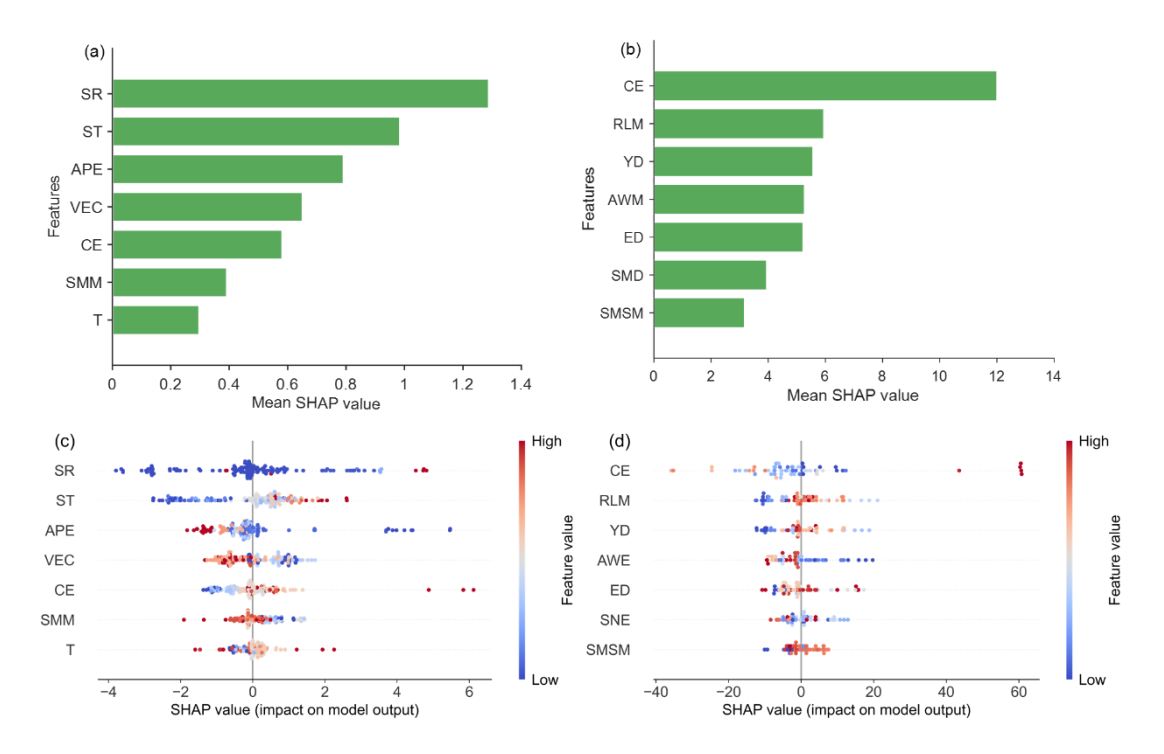


Fig. 11. Global interpretation of our model by SHAP values. (a) SHAP feature importance for adiabatic temperature change. (b) SHAP feature importance for average stress hysteresis. (c) The SHAP values with samples for adiabatic temperature change. (d) The SHAP values with samples for average stress hysteresis.

**Fig. 11** provides a visual representation of the distribution of SHAP values across the samples. The magnitude of the absolute SHAP value indicates the impact of a feature on the output. A larger absolute value gives rise to a stronger influence on the outputs. Additionally, positive SHAP values tend to increase the output, while negative SHAP values indicate a tendency to lower the values of the output. From **Fig. 11 (a)**,

the feature with the most significant impact on adiabatic temperature change is SR, while the least influential is T. The ranking of feature importance for the adiabatic temperature change is SR > ST > APE > VEC > CE > SMM > T. According to Fig. 11 (b), CE is the most significant feature affecting the stress hysteresis, whereas SMSM is the least influential feature. The ranking of feature importance for stress hysteresis is CE > RLM > YD > AWM > ED > SMD > SMSM. As shown in Fig. 11 (c) and Fig. 11 (d), the abscissa describes the feature values of the sample numbers, while the ordinate depicts the corresponding SHAP values. A common color code is used, with blue typically denoting lower feature values and red indicating higher feature values. Positive SHAP values denote the positive impact of the feature value on output, while negative values indicate the opposite. A SHAP value of zero suggests that the corresponding feature does not influence the sample. Comparing the SHAP values and feature values offers a promising approach to understanding the effect of each feature on adiabatic temperature change and hysteresis.

As shown in Fig. 12, the vertical axis describes the values of each feature, whereas the horizontal axis describes the corresponding SHAP value. The pink color indicates a low feature value, and the yellow color indicates a high feature. SR and ST are important parameters for testing adiabatic temperature changes, which represent strain rate and applied maximum stress. From Fig.12 (a) and (b), as the feature values of SR and ST increase, the corresponding SHAP values of SR and ST continuously increase. High strain rates and stress values play a pivotal role in promoting the elastocaloric effect, while their reduction can suppress this effect. This is attributed to the fact that high strain rates facilitate the creation of adiabatic environments, where heat transfer is minimized, while elevated stress levels enable a complete martensitic phase transformation. Our results align with the previous studies conducted by Schmidt et al. [94] and Tušek et al. [95]. The Atomic packing efficiency, APE, compares the ratio of the radii of the central atom to neighboring atoms with the ideal radii ratio of an optimally-packed cluster containing the same number of atoms. [96]. As the difference between the ratios increases, APE rises as well. Remarkably, our findings in Fig. 12 (c)

reveal that negative APE contributes to an increase in the adiabatic temperature change, whereas a positive APE value leads to a decrease in the adiabatic temperature change. Based on this observation, we deduce that an increase in APE results in an elevated ratio of inner atomic radius to outer atomic radius. This will increase the unoccupied space within the clusters, which may result in lower lattice compatibility and higher plastic strain accumulation. Consequently, it affects adiabatic capacity negatively.

VEC refers to valence electron concentration, which serves as a significant parameter in first-principles band calculations for phase selection rules [97, 98]. The influence of VEC on the structural transformation and mechanical properties of alloys has been extensively studied and documented. For instance, it has been observed that both the martensite start temperature  $(M_s)$  and austenite finish temperature  $(A_f)$  decrease as the valence electron concentration increases [98]. Fig. 12 (d) illustrates a declining trend in the SHAP values with increasing VEC. Furthermore, VEC values below 9 positively impact the adiabatic temperature change, whereas they exhibit a negative influence when the VEC exceeds 9. This result bears resemblance to the phase selection rules commonly observed in high-entropy alloys, where VEC values below 6.87 favor the stability of the BCC phase [99]. CE is the configurational entropy, which is a very important thermodynamic parameter that describes the degree of disorder in the state of a mixed system [100-102]. In general, high CE values contribute to the extent of disorder in an alloy system and lower the tendency of ordering and segregation of alloy elements. In other words, high CE values stabilize the formation of the solid-solution phase, while low CE enables intermetallic compounds/secondary phases to form more easily. As depicted in Fig. 12 (e), there is a decreasing trend in the SHAP values with increasing CE. This can be attributed to the fact that high mixing entropy leads to higher lattice distortions and modifications to the Thermodynamic driving force, thereby influencing the inverse martensitic phase transformation. Plastic strain that accumulates due to high local lattice distortions, causes energy dissipation, thus, lower adiabatic temperature change. The shear mean modulus (SMM) is associated with the interaction forces between atoms [103]. In general, elevated shear modulus values indicate robust

chemical bonds and significant resistance to shape alterations. As shown in Fig. 12 (f), with SMM increase, its influence on adiabatic temperature change shifts from promotion to inhibition, possibly due to stringing bonding delaying the phase transformation. Lastly, it can be observed from Fig. 12 (g) that high test temperature (T) tends to have a positive effect on adiabatic temperature changes, although data slightly deviates from this trend.

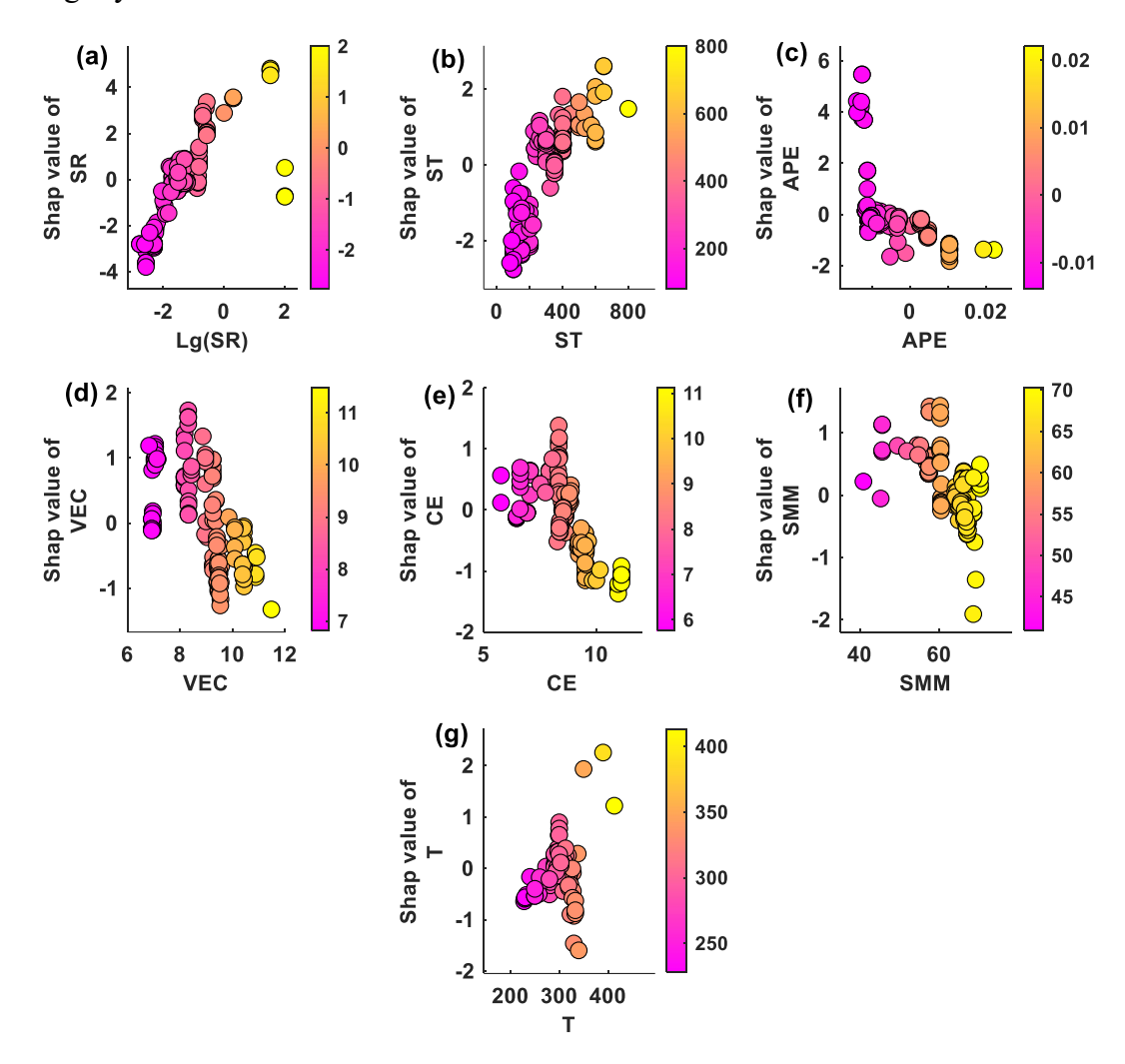


**Fig. 12.** Feature independence plots for adiabatic temperature change showing the SHAP values as a function of a pair of the seven features. The color bars represent the values of features. (a) Strain rate. (b) Stress. (c) Atomic packing efficiency. (d) Valance electron concentration. (e)

Configuration entropy. (f) Shear modulus mean. (g) Test temperature.

The SHAP values of feature dependence for hysteresis are presented in **Fig. 13**. As the CE increases, the overall tendency of SHAP values shifts from negative to positive. High CE facilitates the formation of solid solution phases and results in greater

lattice disorder. Crystal defects have the potential to disrupt the crystal structure of B2 and lead to incompatible martensitic phase transformations. Subsequently, incompatibility can decrease middle eigenvalue  $\lambda_2$  and increase energy loss leading to a rise in stress hysteresis in Fig. 13 (a). The RLM, or radii local mismatch, quantifies the disparities in atomic sizes [101]. It is well known that the lattice distortion and diffusion of atoms in the matrix are affected by the atomic size differences. Large radii differences increase the local strain energy and free energy in the alloy system, but also decrease the diffusion rate in the matrix and could result in local atom segregation. According to Fig. 13 (b), Our calculations indicate that while a low RLM negatively affects the hysteresis of the alloy, and a high RLM generally has a positive effect on the hysteresis, the impact of RLM is not linear. This may suggest that lattice distortion due to RLM can obstruct dislocation movements and create lattice incompatibility. These two outcomes have opposite impacts on hysteresis; therefore, an optimal value of RLM exists [104]. The YD is an important phase formation parameter, which describes the comprehensive effect of the atomic size difference in the n-element alloy. As shown in Fig. 13 (c), the SHAP value of YD is similar to the RLM in this work. AWM is the mean atomic weight. It is interesting to see from Fig. 13 (d) that the SHAP values decrease with AWM. This suggests that the addition of heavy elements can significantly reduce the stress hysteresis in the alloy. ED is the difference of electronegativity [101], which is associated with elemental segregation [55, 99]. ED has been used to determine the phase selection in high entropy alloys. As depicted in Fig. 13 (e), ED shows no significant effect on stress hysteresis. The SMD represents the difference in shear modulus, which reflects the elastic interaction between atoms [105]. It is interesting to see from Fig. 13 (f) that high SMD tends to decrease stress hysteresis. SMSM, or modulus mismatch in the strengthening model, is utilized to forecast the hardness in high entropy alloys. In Fig. 13 (g), with the SMSM increase, the SHAP value first increases and then decreases. This suggests high modulus mismatch between elements tend to reduce phase compatibility during the martensitic transformation. In addition, feature dependence plots of adiabatic temperature change and stress hysteresis are showed in Supplementary information.

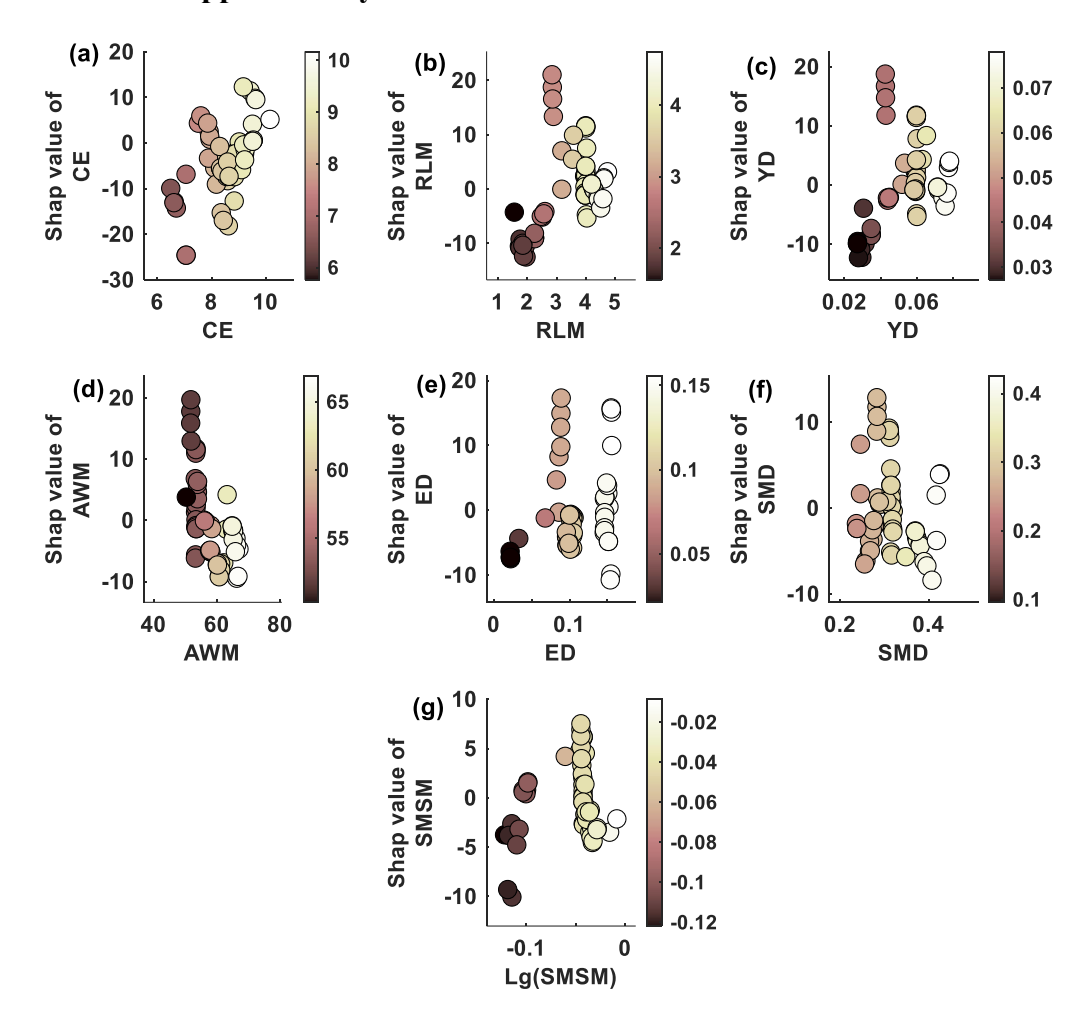


Fig. 13. Feature independence plots for average stress hysteresis showing the SHAP values as a function of a pair of the seven features. The color bars represent the values of features. (a)

Configuration entropy. (b) Radii local mismatch. (c) Yang delta. (d) Mean atomic weight. (e)

Electronegativity delta. (f) Shear modulus delta. (g) Shear modulus strength model

4.2 Interpreting the machine learning model by SISSO

The SHAP method facilitates the analysis of the relationship between selected features and alloy properties. However, it does not provide an explicit expression for this relationship. SISSO is a symbolic regression method, which defines appropriate combinations of mathematical operators that analytically relate the selected features with the outputs using an optimization method. Compared with the black-box model, in this "white-box" model based on SISSO, it is easy to interpret the relationships between inputs and outputs and accelerate the development of novel materials.

However, when dealing with an extensive array of variables, SISSO demands significant computational resources and becomes challenging to identify pivotal features and associated mathematical expressions. We propose a combined strategy that uses the key feature combination from our black-box model and is merged with SISSO to achieve an interpretable ML model. Cross-validation with "leave-one-out" is used to evaluate the performance of SISSO. We use operators  $\Theta = (+, -, \times, \div, \exp, \ln, \sqrt{\cdot^{-1, -2}, \cdot^{-3}})$  merging with the selected features to generate enough descriptor spaces  $\psi_{i \in N}$  with specific complexity. Particle swarm optimization is employed to search for the optimal descriptor combination from a pool of millions of descriptors. The formula for adiabatic temperature change and average stress hysteresis are expressed as Eq (2) and Eq (3), respectively:

$$\Delta T_{ad} = -6.46 \frac{SR^{-1} - ST}{VEC^3} - 4.86APE(SMM - SR)\sqrt{SR}$$

$$+3514.68 \left(\frac{CE}{ln(SMM)} - \frac{1}{T}\right)$$

$$+0.015 \frac{T}{ST(APE * VEC - CE)} + 22.97(2)$$

$$\Delta \sigma_{hy} = +20.58 \frac{ED}{CE \cdot AWM + SNE - CE} + 4.28 \frac{SMSM}{ED^2 + CE \cdot RLM}$$

$$+34.58 \frac{ED}{ED + SNE - RML^3} + 12.09 \frac{SMSM}{CE \cdot AWM, + \sqrt{ED}}$$

$$-16.59 \frac{RLM}{ED^{-1} - RLM^3} + 0.16 \frac{ED}{YD + SMSM - \frac{YD}{RLM}} + 45.77 (3)$$

Where the  $\triangle T_{ad}$  is the absolute value of adiabatic temperature change during the cooling process, the  $\triangle \sigma_{hy}$  is the average stress hysteresis. The  $\frac{SR^{-1}-ST}{VEC^3}$  and  $\frac{ED}{CE \cdot AWM + SNE-CE}$  are the symbolic operators.

As shown in **Fig. 14**, the data points are distributed in proximity to the diagonal line. For adiabatic temperature change, the RMSE is 2.13 with an R of 0.90, while for average stress hysteresis, the RMSE is 20.00 with an R of 0.94. The results suggest good agreement between predictions and experiments.

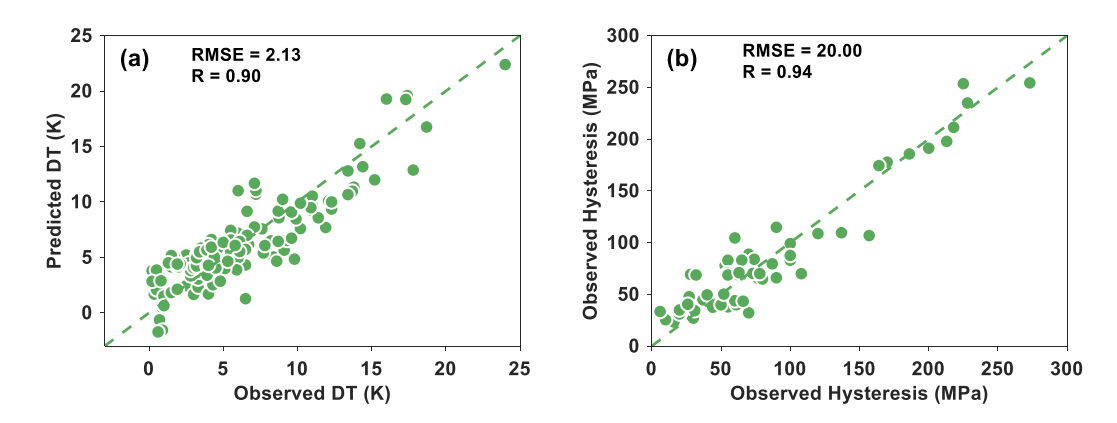


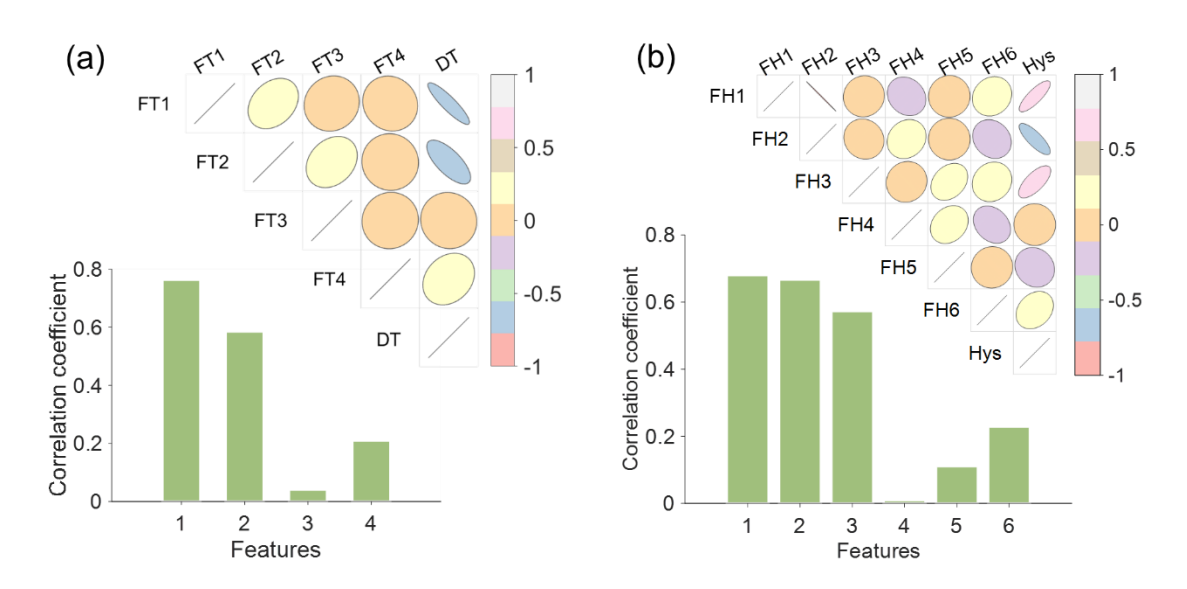
Fig. 14. The cross-validation for  $\triangle T_{ad}$ -SISSO and  $\triangle \sigma_{hy}$ -SISSO model. (a) Adiabatic temperature change. (b) Average stress hysteresis.

Table. 2. The representations for FTX and FHY.

FTX	Operators	FHY	Operators
FT1	$\frac{SR^{-1} - ST}{VEC^3}$	FH1	$\frac{ED}{CE \cdot AWM + SNE - CE}$
FT2	$APE(SMM - SR)\sqrt{SR}$	FH2	$\frac{SMSM}{ED^2 + CE \cdot RLM}$
FT3	$\frac{CE}{ln(SMM)} - \frac{1}{T}$	FH3	$\frac{ED}{ED + SNE - RML^3}$
FT4	$\frac{T}{ST(APE*VEC-CE)}$	FH4	$\frac{SMSM}{CE \cdot AWM, +\sqrt{ED}}$
-	-	FH5	$\frac{RLM}{ED^{-1} - RLM^3}$
-	-	FH6	$\frac{ED}{YD + SMSM - \frac{YD}{RLM}}$

According to Eq (2) and (3), the adiabatic temperature change demonstrates an increasing trend with ST and SR, while it exhibits a decreasing trend with APE. The average stress hysteresis showcases a reduction with AWM, aligning with the findings derived from the SHAP method. These discoveries reinforce the concurrence of results from the SHAP method. Eq (3) also indicates that the additions of heavy elements contribute to obtaining small stress hysteresis. As shown in **Table 2**, the operators are marked as new features FTX and FHY (X, Y are 1 2 3, ...) for adiabatic temperature change and average stress hysteresis, respectively. We also use Pearson correlation to analyze the importance of these operators. **Fig. 15 (a)** shows the correlation coefficient between FTX and  $\triangle T_{\rm ad}$ . The operator most strongly correlated with adiabatic temperature change is FT1, with a correlation coefficient exceeding 0.7. Conversely, FT3 exhibits the weakest correlation, with a coefficient below 0.1. As shown in **Fig. 15** 

**(b)**, FH1 demonstrates the most robust correlation with average stress hysteresis, exhibiting a correlation coefficient exceeding 0.6. In contrast, FH4 displays the weakest correlation, with a coefficient falling close to 0. Furthermore, there is no discernible correlation among the operators for FHX and FHY. In summary, the utilization of analytical expressions enhances the understanding of how material features affect their transformation behavior.



**Fig. 15**. Correlation matrix between operators and properties. (a) Adiabatic temperature change. (b) Average stress hysteresis.

#### 5. Conclusion

In this work, we presented a machine learning framework for efficiently evaluating the adiabatic temperature change and average stress hysteresis in shape memory alloys that accelerate the development of alloys with large elastocaloric effects and low stress hysteresis. More specifically, the conclusions from our work are as follows:

- (1) The key features for each property were identified by using recursive feature elimination and exhaustive search elimination. The ranking of feature importance for the adiabatic temperature change is SR > ST > APE > VEC > CE > SMM > T. The ranking of feature importance for stress hysteresis is CE > RLM > YD > AWM > ED > SMD > SMSM.
- (2) The XGBT model yields the best performance for predicting adiabatic temperature change, achieving an RMSE of 1.75 K. Meanwhile, for predicting stress

hysteresis, the SVR model exhibits good performance with an RMSE of 23.4 MPa.

- (3) Leveraging our trained machine learning model in conjunction with a Bayesian optimization algorithm, a novel alloy Ti<sub>49.3</sub>Ni<sub>45.9</sub>Cu<sub>3.7</sub>Co<sub>1.0</sub>Zr<sub>0.1</sub> has been developed with large adiabatic temperature change and low average stress hysteresis ( $\triangle T_{ad} = 15.2 \text{ K}$ ,  $\triangle \sigma_{hy} = 70.3 \text{ MPa}$ ). These measurements are consistent with our predictions ( $\triangle T_{ad} = 16.8 \text{ K}$ ,  $\triangle \sigma_{hy} = 83.1 \text{ MPa}$ ), corroborating the accuracy of our model.
- (4) The SHAP method was used to interpret the implicit relationship between the input key features and properties. Except for the features representing specific experimental conditions, like strain rate, the most crucial alloy features APE, CE, and RLM are attributed to changes in lattice compatibility, local lattice distortion and chemical driving force in the alloy.
- (5) Based on the selected key feature group, the operators generated by the SISSO method were used to construct analytical expressions for the adiabatic temperature change and average stress hysteresis using key features as variables. The new descriptor agreed well with the results from the SHAP method.

In summary, the present computational framework serves as a starting platform for high-throughput material discovery and optimization, and it holds the potential to play a pivotal role in the systematic design of novel elastocaloric alloys with desired properties. This in turn will facilitate the fast development of non-vapor compression machines that will help to realize carbon-neutral refrigeration technologies.

#### **Acknowledgments**

This work was funded by the National Natural Science Foundation of China (No. 52022055, 52031005, 52211530096). This work was also supported by the Science and Technology Commission of Shanghai Municipality (No. 20DZ2220400), the Open Project of State Key Laboratory for Modification of Chemical Fibers and Polymer Materials (No. KF2206), the State Key Laboratory of Robotics (No. 2023-O19) and the Osaka University's International Joint Research Promotion Program. The authors would also like to thank the Royal Society for the funding, via the International Exchanges

## **Data availability**

Data will be made available on request.

#### References

- [1] B. Li, Y. Kawakita, S. Ohira-Kawamura, T. Sugahara, H. Wang, J. Wang, Y. Chen, S.I. Kawaguchi, S. Kawaguchi, K. Ohara, Colossal barocaloric effects in plastic crystals, Nature 567(7749) (2019) 506-510.
- [2] S. Qian, Y. Geng, Y. Wang, J. Ling, Y. Hwang, R. Radermacher, I. Takeuchi, J. Cui, A review of elastocaloric cooling: Materials, cycles and system integrations, International Journal of Refrigeration 64 (2016) 1-19.
- [3] J. Quarini, A. Prince, Solid state refrigeration: Cooling and refrigeration using crystalline phase changes in metal alloys, Proceedings of the Institution of Mechanical Engineers, Part C: Journal of Mechanical Engineering Science 218(10) (2004) 1175-1179.
- [4] A. Greco, C. Aprea, A. Maiorino, C. Masselli, A review of the state of the art of solid-state caloric cooling processes at room-temperature before 2019, International Journal of Refrigeration 106 (2019) 66-88.
- [5] L. Pfeuffer, J. Lemke, N. Shayanfar, S. Riegg, D. Koch, A. Taubel, F. Scheibel, N.A. Kani, E. Adabifiroozjaei, L. Molina-Luna, K.P. Skokov, O. Gutfleisch, Microstructure engineering of metamagnetic Ni-Mn-based Heusler compounds by Fe-doping: A roadmap towards excellent cyclic stability combined with large elastocaloric and magnetocaloric effects, Acta Materialia 221 (2021).
- [6] L. Manosa, A. Planes, Materials with Giant Mechanocaloric Effects: Cooling by Strength, Adv Mater 29(11) (2017) 1603607.
- [7] H. H. Wu, J. Zhu, T.-Y. Zhang, Double hysteresis loops and large negative and positive electrocaloric effects in tetragonal ferroelectrics, Physical Chemistry Chemical Physics 17(37) (2015) 23897-23908.
- [8] H. H. Wu, J. Zhu, T.-Y. Zhang, Pseudo-first-order phase transition for ultrahigh positive/negative electrocaloric effects in perovskite ferroelectrics, Nano Energy 16 (2015) 419-427.
- [9] F. Xiao, A. Bucsek, X. Jin, M. Porta, A. Planes, Giant elastic response and ultra-stable elastocaloric effect in tweed textured Fe-Pd single crystals, Acta Materialia 223 (2022) 117486.
- [10] P. Dang, F. Ye, Y. Zhou, L. Ding, J. Pang, L. Zhang, X. Ding, J. Sun, S. Dai, T. Lookman, D. Xue, Low-fatigue and large room-temperature elastocaloric effect in a bulk Ti49.2Ni40.8Cu10 alloy, Acta Materialia 229 (2022) 117802.
- [11] Y. Cheng, Y.-Y. Ting, C.-H. Chen, Superelasticity and elastocaloric effect of Ti-rich TiNi shape memory ribbon, Materials Science and Engineering: A 855 (2022) 143945.
- [12] M. Imran, X. Zhang, Recent developments on the cyclic stability in elastocaloric materials, Materials & Design 195 (2020) 109030.
- [13] S. Qian, D. Catalini, J. Muehlbauer, B. Liu, H. Mevada, H. Hou, Y. Hwang, R. Radermacher, I. Takeuchi, High-performance multimode elastocaloric cooling system, Science 380(6646) (2023) 722-727.
- [14] F. Masdeu, J. Pons, J. Torrens-Serra, Y. Chumlyakov, E. Cesari, Superelastic behavior and

- elastocaloric effect in a Ni51.5Fe21.5Ga27.0 ferromagnetic shape memory single crystal under compression, Materials Science and Engineering: A 833 (2022) 142362.
- [15] C. Liu, Z. Li, H. Wang, Y. Wang, B. Yang, H. Yan, D. Cong, X. Zhao, L. Zuo, Long-Term Stable Elastocaloric Effect in a Heusler-Type Co51V33Ga16 Polycrystalline Alloy, ACS Applied Energy Materials 5(10) (2022) 12953-12965.
- [16] Y. Zhu, H. Xuan, J. Su, F. Chen, K. Zhang, P. Han, J. Qiao, Large elastocaloric effect in as-cast Ni-Mn-Sn-Fe ferromagnetic shape memory alloys, Physics Letters A 451 (2022) 128374.
- [17] H. Ossmer, C. Chluba, M. Gueltig, E. Quandt, M. Kohl, Local evolution of the elastocaloric effect in TiNi-based films, Shape Memory and Superelasticity 1 (2015) 142-152.
- [18] H. Ossmer, F. Lambrecht, M. Gültig, C. Chluba, E. Quandt, M. Kohl, Evolution of temperature profiles in TiNi films for elastocaloric cooling, Acta Materialia 81 (2014) 9-20.
- [19] C. Bechtold, C. Chluba, D. Lima, E. Quandt, High cyclic stability of the elastocaloric effect in sputtered TiNiCu shape memory films, Applied Physics Letters 101(9) (2012) 125901-78.
- [20] X. Zhang, H. Chen, S. Li, Y. Niu, T. Yin, C. Song, R. Lang, D. Cong, S. Li, Y.-D. Wang, Enhanced cyclability of superelasticity and elastocaloric effect in Cu and B co-doped Co-Ni-Ga shape memory alloys, Journal of Alloys and Compounds 918 (2022) 165633.
- [21] B. Yuan, S. Zhong, M. Qian, X. Zhang, L. Geng, Elastocaloric effect in bamboo-grained Cu71.1Al17.2Mn11.7 microwires, Journal of Alloys and Compounds 850 (2021) 156612.
- [22] L. Mañosa, S. Jarque-Farnos, E. Vives, A. Planes, Large temperature span and giant refrigerant capacity in elastocaloric Cu-Zn-Al shape memory alloys, Applied Physics Letters 103(21) (2013).
- [23] Y. Chen, X. Zhang, D.C. Dunand, C.A. Schuh, Shape memory and superelasticity in polycrystalline Cu–Al–Ni microwires, Applied Physics Letters 95(17) (2009) 171906.
- [24] L. Brown, The thermal effect in pseudoelastic single crystals of  $\beta$ -CuZnSn, Metallurgical and Materials Transactions A 12 (1981) 1491-1494.
- [25] C. Rodriguez, L. Brown, The thermal effect due to stress-induced martensite formation in β-CuAlNi single crystals, Metallurgical and Materials Transactions A 11 (1980) 147-150.
- [26] J. He, Z. Wei, W. Sun, X. Lu, S. Ma, J. Liu, Martensitic transformation and elastocaloric effect of Co51.5+V31.5-Ga17 (x = 0.1, 0.2, 0.3) alloys, Intermetallics 139 (2021).
- [27] L. Peltier, P. Lohmuller, F. Meraghni, E. Patoor, P. Laheurte, S. Berveiller, Damping Behavior in a Wide Temperature Range of FeMn-Like High Entropy Shape Memory Alloys, Shape Memory and Superelasticity (2022) 335-348.
- [28] D. Cong, W. Xiong, A. Planes, Y. Ren, L. Manosa, P. Cao, Z. Nie, X. Sun, Z. Yang, X. Hong, Y. Wang, Colossal Elastocaloric Effect in Ferroelastic Ni-Mn-Ti Alloys, Phys Rev Lett 122(25) (2019) 255703.
- [29] Z. Yang, D. Cong, Y. Yuan, R. Li, H. Zheng, X. Sun, Z. Nie, Y. Ren, Y. Wang, Large room-temperature elastocaloric effect in a bulk polycrystalline Ni-Ti-Cu-Co alloy with low isothermal stress hysteresis, Applied Materials Today 21 (2020) 100844.
- [30] L. Wang, H. Xuan, S. Liu, T. Cao, Z. Xie, X. Liang, F. Chen, K. Zhang, L. Feng, P. Han, Y. Wu, Enhanced elastocaloric effect and mechanical properties of Gd-doped Ni–Mn–Sn-Gd ferromagnetic shape memory alloys, Journal of Alloys and Compounds 846 (2020).
- [31] H. Xuan, T. Cao, S. Liu, L. Wang, Z. Xie, X. Liang, F. Chen, P. Han, The effect of Co on elastocaloric and mechanical properties of Ni-Co-Mn-Al alloys, Solid State Communications 301 (2019).
- [32] Y. Shen, W. Sun, Z.Y. Wei, Q. Shen, Y.F. Zhang, J. Liu, Orientation dependent elastocaloric effect in directionally solidified Ni-Mn-Sn alloys, Scripta Materialia 163 (2019) 14-18.

- [33] T. Cao, H. Xuan, S. Liu, L. Wang, Z. Xie, X. Liang, F. Chen, P. Han, D. Wang, Y. Du, Enhanced elastocaloric effect and mechanical properties of Fe-doped Ni–Mn–Al ferromagnetic shape memory alloys, Intermetallics 112 (2019).
- [34] Y. Kim, M.-G. Jo, J.-W. Park, H.-K. Park, H.N. Han, Elastocaloric effect in polycrystalline Ni 50 Ti 45.3 V 4.7 shape memory alloy, Scripta Materialia 144 (2018) 48-51.
- [35] F. Bruederlin, L. Bumke, C. Chluba, H. Ossmer, E. Quandt, M. Kohl, Elastocaloric Cooling on the Miniature Scale: A Review on Materials and Device Engineering, Energy Technology 6(8) (2018) 1588-1604.
- [36] S.-M. Kirsch, F. Welsch, N. Michaelis, M. Schmidt, A. Wieczorek, J. Frenzel, G. Eggeler, A. Schütze, S. Seelecke, NiTi-Based Elastocaloric Cooling on the Macroscale: From Basic Concepts to Realization, Energy Technology 6(8) (2018) 1567-1587.
- [37] H. Zhang, J. Liu, Z. Ma, Y. Ren, D. Jiang, L. Cui, K. Yu, Small stress-hysteresis in a nanocrystalline TiNiCuFe alloy for elastocaloric applications over wide temperature window, Journal of Alloys and Compounds 928 (2022) 167195.
- [38] H. Hou, E. Simsek, T. Ma, N.S. Johnson, S. Qian, C. Cisse, D. Stasak, N. Al Hasan, L. Zhou, Y. Hwang, R. Radermacher, V.I. Levitas, M.J. Kramer, M.A. Zaeem, A.P. Stebner, R.T. Ott, J. Cui, I. Takeuchi, Fatigue-resistant high-performance elastocaloric materials made by additive manufacturing, Science 366(6469) (2019) 1116-1121.
- [39] O. Karakoc, C. Hayrettin, A. Evirgen, R. Santamarta, D. Canadinc, R. Wheeler, S. Wang, D. Lagoudas, I. Karaman, Role of microstructure on the actuation fatigue performance of Ni-Rich NiTiHf high temperature shape memory alloys, Acta Materialia 175 (2019) 107-120.
- [40] R. Delville, H. Shi, R.D. James, D. Schryvers, Special microstructures and twin features in Ti50Ni50-X (Pd, Au) X at small hysteresis, Solid State Phenomena 172 (2011) 105-110.
- [41] M. Schmidt, J. Ullrich, A. Wieczorek, J. Frenzel, A. Schütze, G. Eggeler, S. Seelecke, Thermal Stabilization of NiTiCuV Shape Memory Alloys: Observations During Elastocaloric Training, Shape Memory and Superelasticity 1(2) (2015) 132-141.
- [42] H. Chen, F. Xiao, X. Liang, Z. Li, X. Jin, T. Fukuda, Stable and large superelasticity and elastocaloric effect in nanocrystalline Ti-44Ni-5Cu-1Al (at%) alloy, Acta Materialia 158 (2018) 330-339.
- [43] G.L.W. Hart, T. Mueller, C. Toher, S. Curtarolo, Machine learning for alloys, Nature Reviews Materials 6(8) (2021) 730-755.
- [44] S. He, X. Liu, Q. Feng, G. Chen, X. Zou, Z. Wu, C. Li, X. Lu, Thermodynamic assessments of ZrO2-YO1. 5-TiO2 system, Ceramics International 47(17) (2021) 23991-24002.
- [45] S.Y. He, Q. S. Feng, B. H. Duan, G. Y. Chen, W. Zhu, C. H. LI, X. G. Lu, Thermodynamic modeling of ZrO2–CaO–TiO2 system, Transactions of Nonferrous Metals Society of China 32(2) (2022) 696-708.
- [46] R. Shi, Applications of CALPHAD (CALculation of PHAse diagram) modeling in organic orientationally disordered phase change materials for thermal energy storage, Thermochimica Acta 683 (2020) 178461.
- [47] C. Wen, Y. Zhang, C. Wang, D. Xue, Y. Bai, S. Antonov, L. Dai, T. Lookman, Y. Su, Machine learning assisted design of high entropy alloys with desired property, Acta Materialia 170 (2019) 109-117.
- [48] C.J. Wilkinson, C. Trivelpiece, R. Hust, R.S. Welch, S.A. Feller, J.C. Mauro, Hybrid machine learning/physics-based approach for predicting oxide glass-forming ability, Acta Materialia 222 (2022). [49] J. Li, B. Xie, L. Li, B. Liu, Y. Liu, D. Shaysultanov, Q. Fang, N. Stepanov, P.K. Liaw, Performance-oriented multistage design for multi-principal element alloys with low cost yet high efficiency, Mater

- Horiz 9(5) (2022) 1518-1525.
- [50] T.Q. Hartnett, V. Sharma, S. Garg, R. Barua, P.V. Balachandran, Accelerated design of MTX alloys with targeted magnetostructural properties through interpretable machine learning, Acta Materialia 231 (2022).
- [51] Y. Pan, P. Zhou, Y. Yan, A. Agrawal, Y. Wang, D. Guo, S. Goel, New insights into the methods for predicting ground surface roughness in the age of digitalisation, Precision Engineering 67 (2021) 393-418.
- [52] Y. Pan, Y. Qiao, Y. Wang, X. Liu, P. Zhou, Real-time prediction of grinding surface roughness based on multi-sensor signal fusion, (2023).
- [53] L. Peltier, S. Berveiller, F. Meraghni, P. Lohmuller, P. Laheurte, Martensite Transformation and Superelasticity at High Temperature of (TiHfZr)74(NbTa)26 High-Entropy Shape Memory Alloy, Shape Memory and Superelasticity 7(2) (2021) 194-205.
- [54] U.M. Kankanamge, J. Reiner, X. Ma, S.C. Gallo, W. Xu, Machine learning guided alloy design of high-temperature NiTiHf shape memory alloys, Journal of Materials Science 57(41) (2022) 19447-19465.
- [55] D. Xue, D. Xue, R. Yuan, Y. Zhou, P.V. Balachandran, X. Ding, J. Sun, T. Lookman, An informatics approach to transformation temperatures of NiTi-based shape memory alloys, Acta Materialia 125 (2017) 532-541.
- [56] D. Xue, P.V. Balachandran, J. Hogden, J. Theiler, D. Xue, T. Lookman, Accelerated search for materials with targeted properties by adaptive design, Nat Commun 7 (2016) 11241.
- [57] E.L. Pang, G.B. Olson, C.A. Schuh, Low-hysteresis shape-memory ceramics designed by multimode modelling, Nature 610(7932) (2022) 491-495.
- [58] L. Tian, Y.Q. Cheng, Z.W. Shan, J. Li, C.C. Wang, X.D. Han, J. Sun, E. Ma, Approaching the ideal elastic limit of metallic glasses, Nat Commun 3 (2012) 609.
- [59] L. Ding, Y. Zhou, Y. Xu, P. Dang, X. Ding, J. Sun, T. Lookman, D. Xue, Learning from superelasticity data to search for Ti-Ni alloys with large elastocaloric effect, Acta Materialia 218 (2021) 117200.
- [60] A.M. Gopakumar, P.V. Balachandran, D. Xue, J.E. Gubernatis, T. Lookman, Multi-objective optimization for materials discovery via adaptive design, Scientific reports 8(1) (2018) 3738.
- [61] A. Solomou, G. Zhao, S. Boluki, J.K. Joy, X. Qian, I. Karaman, R. Arróyave, D.C. Lagoudas, Multi-objective Bayesian materials discovery: Application on the discovery of precipitation strengthened NiTi shape memory alloys through micromechanical modeling, Materials & Design 160 (2018) 810-827.
- [62] Z. Guan, J. Bai, Y. Zhang, S. Sun, J. Gu, X. Liang, Y. Zhang, C. Esling, X. Zhao, L. Zuo, Achieved good mechanical properties and large elastocaloric effect in Ni-Mn-Ti-Cu-B alloy: Experiments and first-principles calculations, Journal of Alloys and Compounds 930 (2023).
- [63] W. Tong, L. Liang, J. Xu, H.J. Wang, J. Tian, L.M. Peng, Achieving enhanced mechanical, pseudoelastic and elastocaloric properties in Ni-Mn-Ga alloys via Dy micro-alloying and isothermal mechanical cyclic training, Scripta Materialia 209 (2022).
- [64] W. Gui, Y. Qu, Y. Cao, Y. Zhao, C. Liu, Q. Zhou, J. Chen, Y. Liu, The effect of Tb substitution for Ni on microstructure, martensitic transformation and cyclic stability of elastocaloric effect in Ni–Mn–Sn magnetic shape memory alloys, Journal of Materials Research and Technology 19 (2022) 4998-5007.
- [65] Y. Feng, J. Gao, M. Zhou, H. Wang, Giant elastocaloric effect induced by lower stress in Ni-Mn-In-Fe ferromagnetic shape memory alloys, Journal of Magnetism and Magnetic Materials 563 (2022).
- [66] Z. Li, Z. Li, Y. Lu, X. Lu, L. Zuo, Enhanced elastocaloric effect and specific adiabatic temperature variation in Ni-Mn-In-Si-Cu shape memory alloys, Journal of Alloys and Compounds 920 (2022).

- [67] M. Imran, X. Zhang, M. Qian, L. Geng, Enhanced working stability of elastocaloric effects in polycrystalline Ni-Fe-Ga dual phase alloy, Intermetallics 136 (2021).
- [68] Y. Niu, H. Chen, X. Zhang, S. Li, D. Cong, T. Ma, S. Li, J. Lin, Y.-D. Wang, Achieving excellent superelasticity and extraordinary elastocaloric effect in a directionally solidified Co-V-Ga alloy, Scripta Materialia 204 (2021).
- [69] H. Xuan, L. Wang, T. Cao, S. Liu, Z. Xie, X. Liang, F. Chen, K. Zhang, L. Feng, P. Han, Y. Wu, Mechanical and elastocaloric effect of Fe and Co co-doped Ni–Mn–Al ferromagnetic shape memory alloys, Physics Letters A 402 (2021).
- [70] K. Liu, Y. Yuan, S. Ma, G. Feng, D. Wan, S. Wang, C. Chen, X. Luo, Z. Zhong, Large elastocaloric effect around room temperature in directionally solidified Co49Fe3V33Ga15 superelastic alloy, Journal of Alloys and Compounds 884 (2021).
- [71] N.Y. Surikov, E.Y. Panchenko, E.E. Timofeeva, A.I. Tagiltsev, Y.I. Chumlyakov, Orientation dependence of elastocaloric effect in Ni50Mn30Ga20 single crystals, Journal of Alloys and Compounds 880 (2021).
- [72] Z. Li, Z. Li, D. Li, J. Yang, B. Yang, D. Wang, L. Hou, X. Li, Y. Zhang, C. Esling, X. Zhao, L. Zuo, Influence of austenite ferromagnetism on the elastocaloric effect in a Ni44.9Co4.9Mn36.9In13.3 metamagnetic shape memory alloy, Applied Physics Letters 115(8) (2019).
- [73] G.J. Pataky, E. Ertekin, H. Sehitoglu, Elastocaloric cooling potential of NiTi, Ni2FeGa, and CoNiAl, Acta Materialia 96 (2015) 420-427.
- [74] B. Lu, P. Zhang, Y. Xu, W. Sun, J. Liu, Elastocaloric effect in Ni45Mn36.4In13.6Co5 metamagnetic shape memory alloys under mechanical cycling, Materials Letters 148 (2015) 110-113.
- [75] Y.J. Huang, Q.D. Hu, N.M. Bruno, J.-H. Chen, I. Karaman, J.H. Ross, J.G. Li, Giant elastocaloric effect in directionally solidified Ni–Mn–In magnetic shape memory alloy, Scripta Materialia 105 (2015) 42-45.
- [76] C. Chluba, W. Ge, R. Lima de Miranda, J. Strobel, L. Kienle, E. Quandt, M. Wuttig, Shape memory alloys. Ultralow-fatigue shape memory alloy films, Science 348(6238) (2015) 1004-7.
- [77] J. Tušek, K. Engelbrecht, R. Millán-Solsona, L. Mañosa, E. Vives, L.P. Mikkelsen, N. Pryds, The Elastocaloric Effect: A Way to Cool Efficiently, Advanced Energy Materials 5(13) (2015).
- [78] S. He, Y. Wang, Z. Zhang, F. Xiao, S. Zuo, Y. Zhou, X. Cai, X. Jin, Interpretable machine learning workflow for evaluation of the transformation temperatures of TiZrHfNiCoCu high entropy shape memory alloys, Materials & Design 225 (2023) 111513.
- [79] H. Zhang, H. Fu, S. Zhu, W. Yong, J. Xie, Machine learning assisted composition effective design for precipitation strengthened copper alloys, Acta Materialia 215 (2021) 117118.
- [80] L. Ward, A. Dunn, A. Faghaninia, N.E. Zimmermann, S. Bajaj, Q. Wang, J. Montoya, J. Chen, K. Bystrom, M. Dylla, Matminer: An open source toolkit for materials data mining, Computational Materials Science 152 (2018) 60-69.
- [81] T. Akiba, S. Sano, T. Yanase, T. Ohta, M. Koyama, Optuna: A next-generation hyperparameter optimization framework, Proceedings of the 25th ACM SIGKDD international conference on knowledge discovery & data mining, 2019, pp. 2623-2631.
- [82] R. Yuan, Y. Tian, D. Xue, D. Xue, Y. Zhou, X. Ding, J. Sun, T. Lookman, Accelerated Search for BaTiO3-Based Ceramics with Large Energy Storage at Low Fields Using Machine Learning and Experimental Design, Adv Sci (Weinh) 6(21) (2019) 1901395.
- [83] S.M. Lundberg, S.I. Lee, A Unified Approach to Interpreting Model Predictions, Adv Neur In 30 (2017).

- [84] A. Wei, H. Ye, Z. Guo, J. Xiong, SISSO-assisted prediction and design of mechanical properties of porous graphene with a uniform nanopore array, Nanoscale Advances 4(5) (2022) 1455-1463.
- [85] J. Cui, Y.S. Chu, O.O. Famodu, Y. Furuya, J. Hattrick-Simpers, R.D. James, A. Ludwig, S. Thienhaus, M. Wuttig, Z. Zhang, Combinatorial search of thermoelastic shape-memory alloys with extremely small hysteresis width, Nature materials 5(4) (2006) 286-290.
- [86] S. Hsieh, S. Wu, A study on ternary Ti-rich TiNiZr shape memory alloys, Materials characterization 41(4) (1998) 151-162.
- [87] H. Lin, K. Lin, S. Chang, C. Lin, A study of TiNiV ternary shape memory alloys, Journal of alloys and compounds 284(1-2) (1999) 213-217.
- [88] F. Xiao, T. Fukuda, T. Kakeshita, Significant elastocaloric effect in a Fe-31.2 Pd (at.%) single crystal, Applied Physics Letters 102(16) (2013).
- [89] L. Mañosa, D. González-Alonso, A. Planes, E. Bonnot, M. Barrio, J.-L. Tamarit, S. Aksoy, M. Acet, Giant solid-state barocaloric effect in the Ni–Mn–In magnetic shape-memory alloy, Nature Materials 9(6) (2010) 478-481.
- [90] A. Shen, D. Zhao, W. Sun, J. Liu, C. Li, Elastocaloric effect in a Co 50 Ni 20 Ga 30 single crystal, Scripta Materialia 127 (2017) 1-5.
- [91] B. Lu, M. Song, Z. Zhou, W. Liu, B. Wang, S. Lu, C. Wu, L. Yang, J. Liu, Reducing mechanical hysteresis via tuning the microstructural orientations in Heusler-type Ni44.8Mn36.9In13.3Co5.0 elastocaloric alloys, Journal of Alloys and Compounds 785 (2019) 1023-1029.
- [92] G. Vazquez, P. Singh, D. Sauceda, R. Couperthwaite, N. Britt, K. Youssef, D.D. Johnson, R. Arróyave, Efficient machine-learning model for fast assessment of elastic properties of high-entropy alloys, Acta Materialia 232 (2022) 117924.
- [93] S.M. Lundberg, S.-I. Lee, A unified approach to interpreting model predictions, Advances in neural information processing systems 30 (2017).
- [94] M. Schmidt, A. Schütze, S. Seelecke, Elastocaloric cooling processes: The influence of material strain and strain rate on efficiency and temperature span, APL Materials 4(6) (2016).
- [95] J. Tušek, A. Žerovnik, M. Čebron, M. Brojan, B. Žužek, K. Engelbrecht, A. Cadelli, Elastocaloric effect vs fatigue life: Exploring the durability limits of Ni-Ti plates under pre-strain conditions for elastocaloric cooling, Acta Materialia 150 (2018) 295-307.
- [96] K.J. Laws, D.B. Miracle, M. Ferry, A predictive structural model for bulk metallic glasses, Nat Commun 6 (2015) 8123.
- [97] D. Piorunek, J. Frenzel, N. Jöns, C. Somsen, G. Eggeler, Chemical complexity, microstructure and martensitic transformation in high entropy shape memory alloys, Intermetallics 122 (2020) 106792.
- [98] M. Zarinejad, Y. Liu, Dependence of Transformation Temperatures of NiTi-based Shape-Memory Alloys on the Number and Concentration of Valence Electrons, Advanced Functional Materials 18(18) (2008) 2789-2794.
- [99] S. Guo, Phase selection rules for cast high entropy alloys: an overview, Materials Science and Technology 31(10) (2015) 1223-1230.
- [100] C. Wen, C. Wang, Y. Zhang, S. Antonov, D. Xue, T. Lookman, Y. Su, Modeling solid solution strengthening in high entropy alloys using machine learning, Acta Materialia 212 (2021).
- [101] Z. Wang, Q. Fang, J. Li, B. Liu, Y. Liu, Effect of lattice distortion on solid solution strengthening of BCC high-entropy alloys, Journal of Materials Science & Technology 34(2) (2018) 349-354.
- [102] Y. Zhang, S. Guo, C.T. Liu, X. Yang, Phase Formation Rules, High-Entropy Alloys2016, pp. 21-49.

- [103] I. Toda-Caraballo, P.E. Rivera-Díaz-del-Castillo, Modelling solid solution hardening in high entropy alloys, Acta Materialia 85 (2015) 14-23.
- [104] M.-H. Tsai, J.-W. Yeh, High-entropy alloys: a critical review, Materials Research Letters 2(3) (2014) 107-123.
- [105] I. Toda-Caraballo, P.E.J. Rivera-Díaz-del-Castillo, Modelling solid solution hardening in high entropy alloys, Acta Materialia 85 (2015) 14-23.